Electronic Supplementary Material (ESI) for Journal of Materials Chemistry A.

Supporting Information

Water vapour and gas induced phase transformations in an 8-fold interpenetrated diamondoid metal-organic framework

Aizhamal Subanbekova,†[a] Varvara I. Nikolayenko,†[a] Andrey A. Bezrukov,[a] Debobroto Sensharma,[a] Naveen Kumar,[a] Daniel J. O'Hearn,[a] Volodymyr Bon,[b] Shi-Qiang Wang,[a,c] Kyriaki Koupepidou,[a] Shaza Darwish,[a] Stefan Kaskel[b] and Michael J. Zaworotko*[a]

[a]Department of Chemical Sciences, Bernal Institute, University of Limerick, Limerick V94T9PX, Republic of Ireland.

[b]Department of Inorganic Chemistry, Faculty of Chemistry and Food Chemistry, Technische Universität Dresden, Bergstrasse 66, 01062 Dresden (Germany)

[c]Institute of Materials Research and Engineering (IMRE), Agency for Science, Technology and Research (A*STAR), 2 Fusionopolis Way 138634, Singapore

†These authors contributed equally.

*Corresponding author. xtal@ul.ie

Contents

1. Materials and Synthesis

All reagents and solvents were procured from Sigma Aldrich and used without further purification. The ligand HImibz = ((4-(1H-Imidazol-1-yl)phenylimino)methyl)benzoic acid was synthesized according to a previously reported literature method.[1]

Bulk synthesis of X-dia-2-Cd-α

A mixture of $Cd(NO_3)_2 \cdot 4H_2O$ (77 mg, 0.25 mmol), HImibz (150 mg, 0.5 mmol) and *N,N*-dimethylformamide (DMF) (3 mL) was added to a 28-mL glass vial and sonicated for 30 seconds. The vial was then sealed and placed in a preheated oven at 105 °C. Crystals formed after 10 hours in the oven, the vial was removed from the oven and allowed to cool to room temperature. Pale brown, plate crystals were harvested by filtration and washed with DMF (yield 58 mg, 34%).

Single crystal synthesis of X-dia-2-Cd-α

X-dia-2-Cd-α was obtained by slow evaporation. $Cd(NO_3)_2 \cdot 4H_2O$ (14 mg, 0.45 mmol) in MeOH (2 ml) was layered over HImibz (12 mg, 0.4 mmol) in DMF (2 ml). The two layers were separated by a DMF-MeOH (1:1) (2 ml) buffer layer. Pale brown crystals were obtained after 1 week. The obtained crystals were used for single crystal X-ray diffraction analysis.

Preparation of X-dia-2-Cd-β

The freshly synthesized **X-dia-2-Cd-α** was filtered, washed with methanol, air dried. Alternatively, **X-dia-2-Cd-β** can be obtained by exchanging DMF with H_2O.

Preparation of X-dia-2-Cd-γ

A bulk sample of **X-dia-2-Cd-γ** was obtained by evacuating the H_2O molecules in **X-dia-2-Cd-β** by heating at 373 K under vacuum. A single crystal X-ray diffraction experiment was performed by heating a crystal of **X-dia-2-Cd-β** to 333 K under a continuous flow of N_2.

2. Single-crystal X-ray diffraction measurements (SCXRD).

Single crystal X-ray diffraction data for **X-dia-2-Cd-α** was collected on a Bruker Quest diffractometer equipped with a CMOS detector and IμS microfocus X-ray source (Cu Kα, λ = 1.54178 Å) under N_2 flow at 100 K. SCXRD data for **X-dia-2-Cd-β** was collected using the same procedure. Crystals of **X-dia-2-Cd-γ** adsorb water from air reverting to the water loaded **X-dia-2-Cd-β** phase. To prevent this, a crystal was glued to a glass capillary and kept under N_2 flow at 333 K.

All SCXRD data were indexed, integrated, and scaled in APEX4.[2] Absorption correction was performed by multi-scan method using SADABS.[3] Space group determination was achieved using XPREP4 implemented in APEX4. Structures were solved using intrinsic phasing method (SHELXT) and refined on F^2 using nonlinear least-squares techniques with SHELXL[4] programs incorporated in X-seed graphical user interface. Anisotropic thermal parameters were applied to all non-hydrogen atoms. Hydrogen atoms were placed in calculated positions using riding models. SCXRD data of **X-dia-2-Cd-α** revealed an 8-fold interpenetrated diamondoid structure. In **X-dia-2-Cd-β,** half of Imibz ligand and aromatic ring are disordered over two positions. The voids space of all the crystal structures was calculated by using PLATON.[5]

Table S1. Selected crystallographic data for three forms of **X-dia-2-Cd.**

	X-dia-2-Cd-α	**X-dia-2-Cd-β**	**X-dia-2-Cd-γ**
Formula	$C_{34}H_{24}N_6O_4Cd$ +solvent	$C_{34}H_{24}N_6O_4Cd$ + solvent	$C_{34}H_{24}N_6O_4Cd$ +0.5 H_2O
Formula weight (g/mol)	693.00	693.00	692.99
Temperature (K)	100	100	333
Wavelength (Å)	1.54056	1.54056	1.54056
Crystal system	Orthorhombic	Orthorhombic	Orthorhombic
Space group	*Pnna*	*Pnna*	*Pnna*
a (Å)	22.6888(9)	17.4659(4)	15.0402(2)
b (Å)	11.2084(4)	15.0647(3)	14.4053(2)
c (Å)	19.6169(8)	13.0708(3)	14.7736(2)
α (°)	90	90	90

β (°)	90	90	90
γ (°)	90	90	90
V (Å^3)	4988.7(3)	3439.17(1)	3200.8(6)
Z	4	4	4
D$_c$ (g/cm^3)	0.923	1.489	1.438
Indexes range	$-27\le h\le 28$, $-12\le k\le 13$, $-24\le l\le 24$	$-21\le h\le 21$, $-15\le k\le 17$, $-15\le l\le 15$	$-16\le h\le 16$, $-15\le k\le 18$, $-17\le l\le 14$
Total reflections	54136	62304	20254
Unique reflections	4945	3287	3048
GooF	1.088	1.067	1.000
R$_1$ [$I > 2\sigma(I)$]	0.0835	0.0490	0.1134
WR$_2$ [all data]	0.2785	0.1592	0.3065
CCDC	2240524	2240522	2240523

The Checkcif **X-dia-2-Cd-β** contains the following alerts:

Alert level B

PLAT306_ALERT_2_B Isolated Oxygen Atom (H-atoms Missing ?)_....... O1B Check

PLAT306_ALERT_2_B Isolated Oxygen Atom (H-atoms Missing ?) .... O1C Check

PLAT430_ALERT_2_B Short Inter D...A Contact O1 ..O1B . 2.75 Ang.

Response: These alerts are associated with the water guest molecules. In spite of multiple attempts, the exact positions of the protons could not be reliably assigned and were left unassigned.

The Checkcif **of X-dia-2-Cd-γ** contains the following alerts:

Alert level A

RINTA01_ALERT_3_A The value of Rint is greater than 0.25 Rint given 0.297

PLAT020_ALERT_3_A The Value of Rint is Greater Than 0.12 .... 0.297 Report

Response: Owing to the hygroscopic nature of this material, the crystal had to be collected at 333 K. This coupled with the significant structural transformations experienced by the crystal in the two previous transformations resulted in a reduction in peak intensity and a high Rint value.

Alert level B

PLAT342_ALERT_3_B Low Bond Precision on C-C Bonds .... 0.024 Ang.

PLAT601_ALERT_2_B Unit Cell Contains Solvent Accessible VOIDS of . 197 Ang**3

Response: Bond precision was reduced owing to a weakly diffracting crystal at a higher than ambient temperature.

3. FTIR spectroscopy

Fourier Transform Infrared (FTIR) spectra were collected on a Perkin Elmer Spectrum 100 spectrometer with Universal Attenuated total reflectance (ATR) accessory between the range of 4000-650 cm^{-1}.

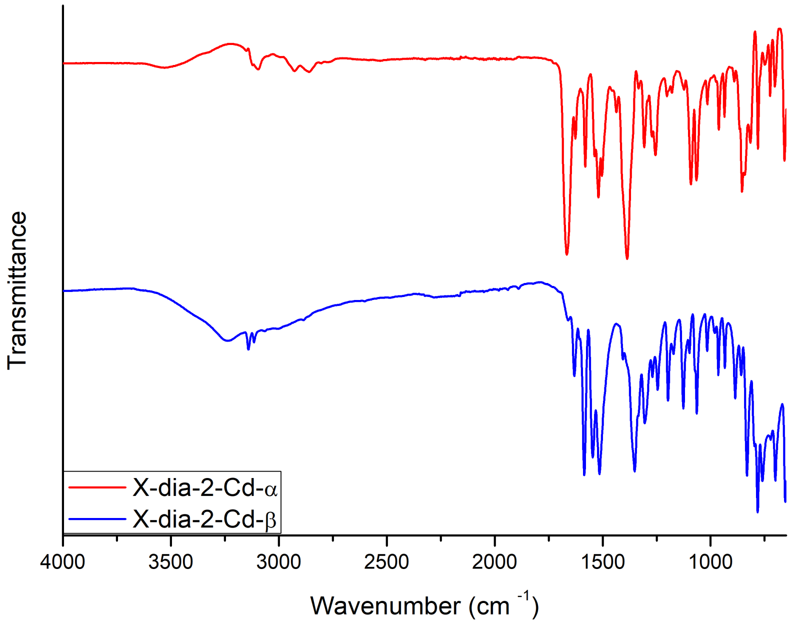

Fig. S1. Overlaid FTIR spectra of ***X-dia-2-Cd-α*** *and* ***X-dia-2-Cd-β****.*

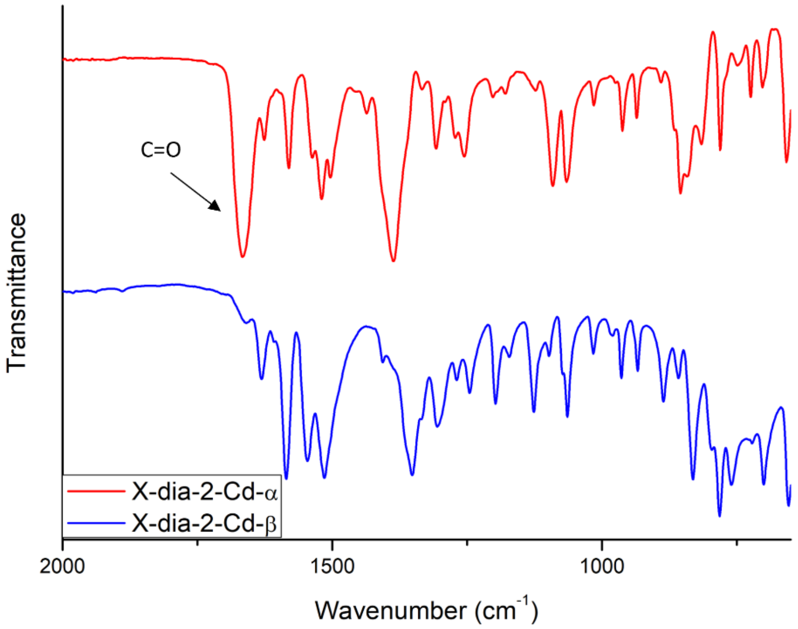

Fig. S2. Zoomed overlay of FTIR spectra ***of X-dia-2-Cd-α*** *and* ***X-dia-2-Cd-β*** *in the range 650-2000 cm*$^{-1}$.

4. Powder X-ray Diffraction (PXRD)

Powder X-ray diffraction (PXRD) experiments were conducted using microcrystalline samples on a PANalytical Empyrean diffractometer (40 kV, 40 mA, Cu $K_{\alpha1,2}$, $\lambda = 1.5418$ Å) in Bragg Brentano geometry. Data was collected from 5 to 40° 2θ with a step size of 0.0262606° and a scan time of 55 seconds per step. Powder samples were evenly distributed on a zero-background Si sample holder after being ground with a mortar and pestle to minimize the effects of preferred orientation. Data analysis was carried out using X'Pert HighScore Plus8 (Version 2.2e).[6] Reference powder patterns were calculated from SCXRD structures using Mercury.[1]

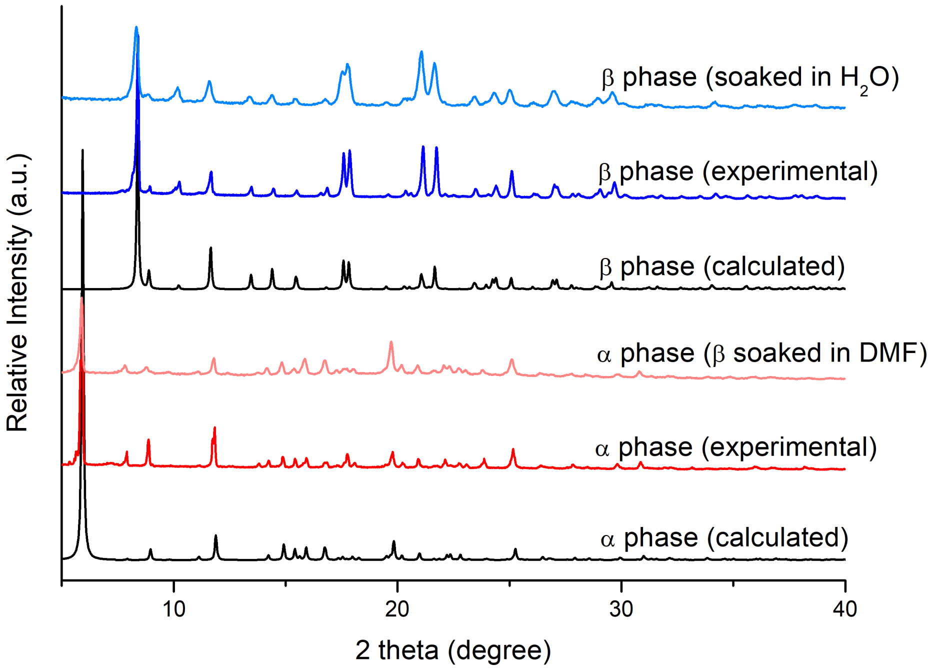

*Fig. S3. Comparison of calculated (black) and experimental PXRD patterns of **X-dia-2-Cd-α** (red) and **X-dia-2-Cd-β** (blue).*

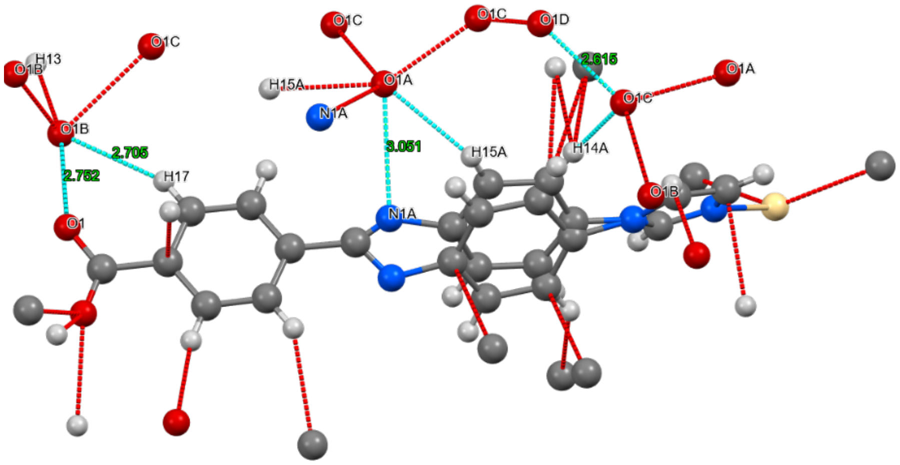

*Fig. S4. Linker disorder and hydrogen bond interactions in asymmetric unit of **X-dia-2-Cd-β**.*

5. Thermogravimetric analysis (TGA)

Thermogravimetric analysis (TGA) was conducted using a TA Instruments Q50 system. Each sample was loaded into an aluminium pan and heated at 10 K min^{-1} from room temperature to 773 K under a continuous flow of N_2.

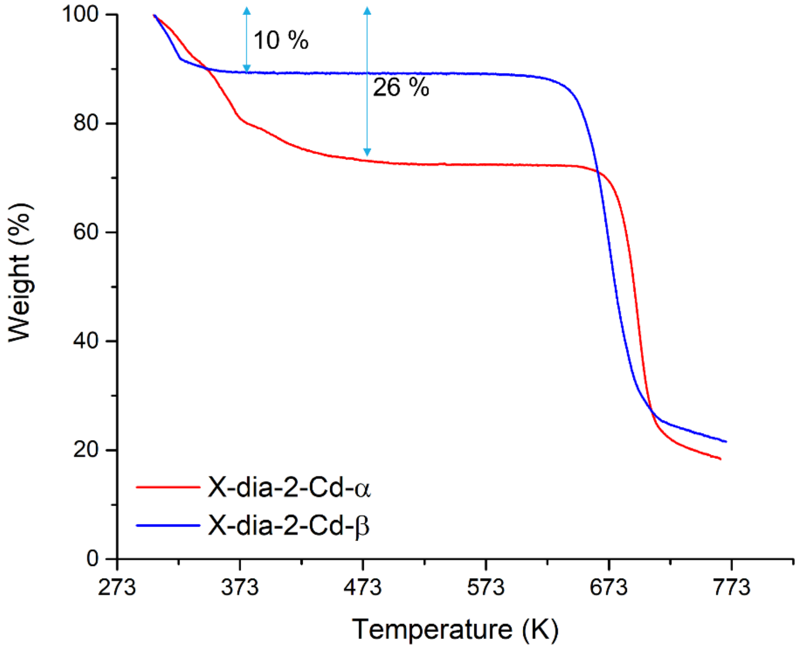

*Fig. S5. Thermogram of **X-dia-2-Cd-α** (red) and **X-dia-2-Cd-β** (blue) under continuous N_2 flow.*

6. Variable Temperature Powder X-ray Diffraction (VT PXRD)

Diffractograms at different temperatures were recorded using a PANalytical X'Pert Pro-MPD diffractometer equipped with a PIXcel3D detector operating in scanning line detector mode. Anton Paar TTK 450 stage coupled with the Anton Paar TCU 110 Temperature Control Unit was used to record the variable temperature diffractograms. The diffractometer is outfitted with an Empyrean Cu LFF (long fine focus) HR (9430 033 7300x) tube operated at 40 kV and 40 mA and CuKα radiation (λ_{α} = 1.54056 Å) was used for diffraction experiments. Continuous scanning mode with the goniometer in the theta-theta orientation was used to collect the data. Incident beam optics included the Fixed Divergences slit, with a 1/4° divergence slit and a Soller slit (0.04 rad). Divergent beam optics included a P7.5 S7 anti-scatter slit, a Soller slit (0.04 rad), and a Ni-β filter. In a typical experiment, 50 mg of sample was ground into a fine powder and was loaded on a zero-background disc made for Anton Paar TTK 450 chamber. The data was collected from 4°-40° (2θ) with a step-size of 0.0167113° and a scan time of 200 seconds per step. Crude data were analysed using the X'Pert HighScore Plus$^{2\text{TM}}$ software V 4.1 (PANalytical, The Netherlands).

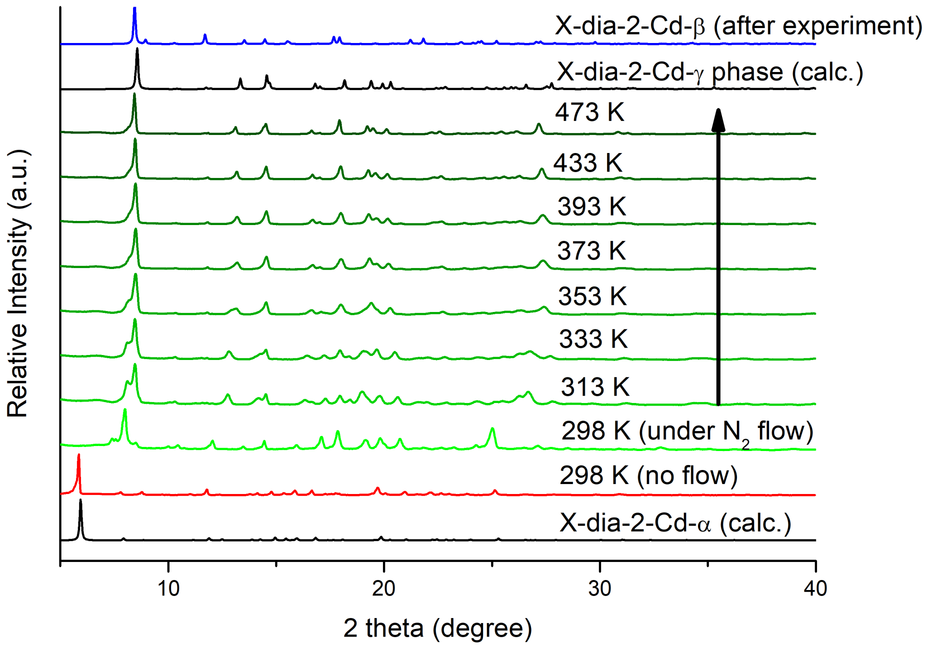

Fig. S6. Overlay of VT-PXRD for X-dia-2-Cd, starting with ***X-dia-2-Cd-α*** *under N$_2$ flow.*

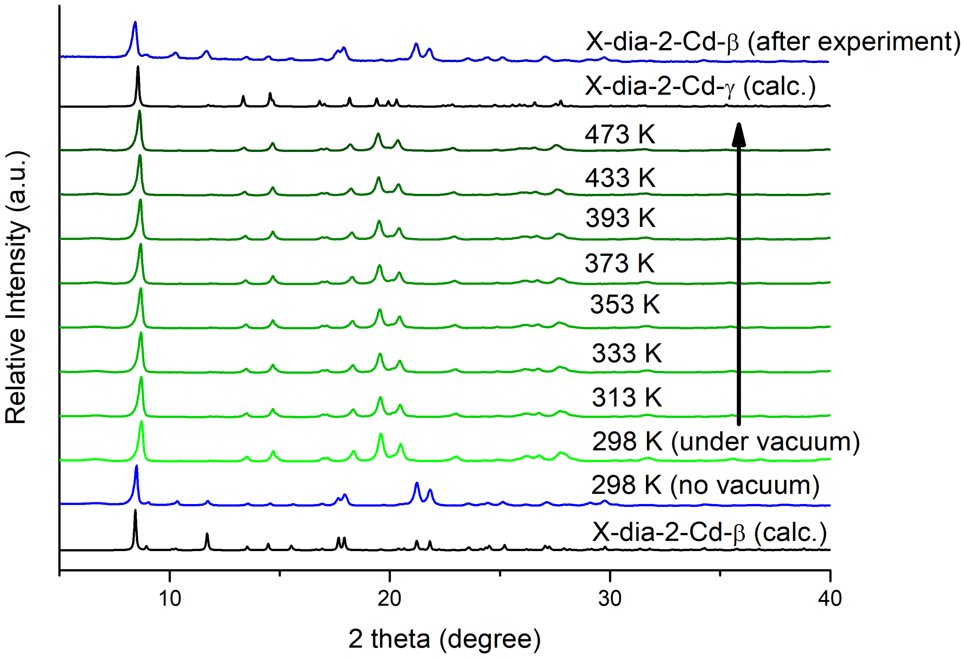

Fig. S7. Overlay of VT-PXRD patterns of ***X-dia-2-Cd*** *starting from* ***X-dia-2-Cd-β*** *under vacuum.*

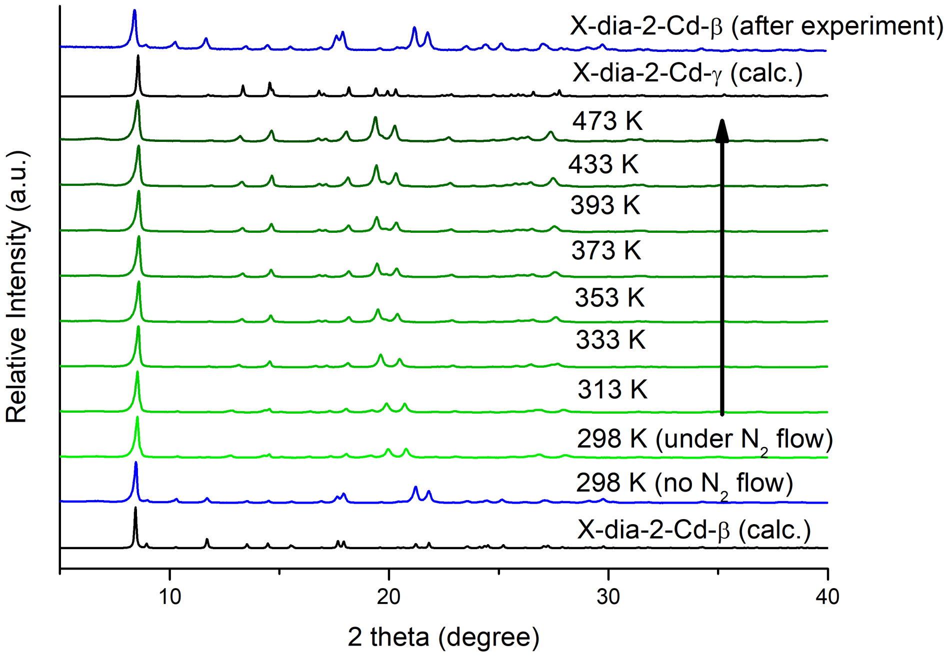

Fig. S8. Overlay of VT-PXRD patterns of ***X-dia-2-Cd*** *starting from* ***X-dia-2-Cd-β*** *under N2 flow.*

Synchrotron powder X-ray diffraction data was collected at beamline I11 at the Diamond Light Source (λ = 0.825978 Å and zero error = 0.0045). Powder sample of beta phase was loaded in a Φ=0.5 mm quartz capillary and connected to dynamic vacuum. Sample was heated from 298 K to 373 K (ramp 5 K/min) using Cryostream Plus while two seconds scans every minute were collected using positional scanning detector (PSD).[7]

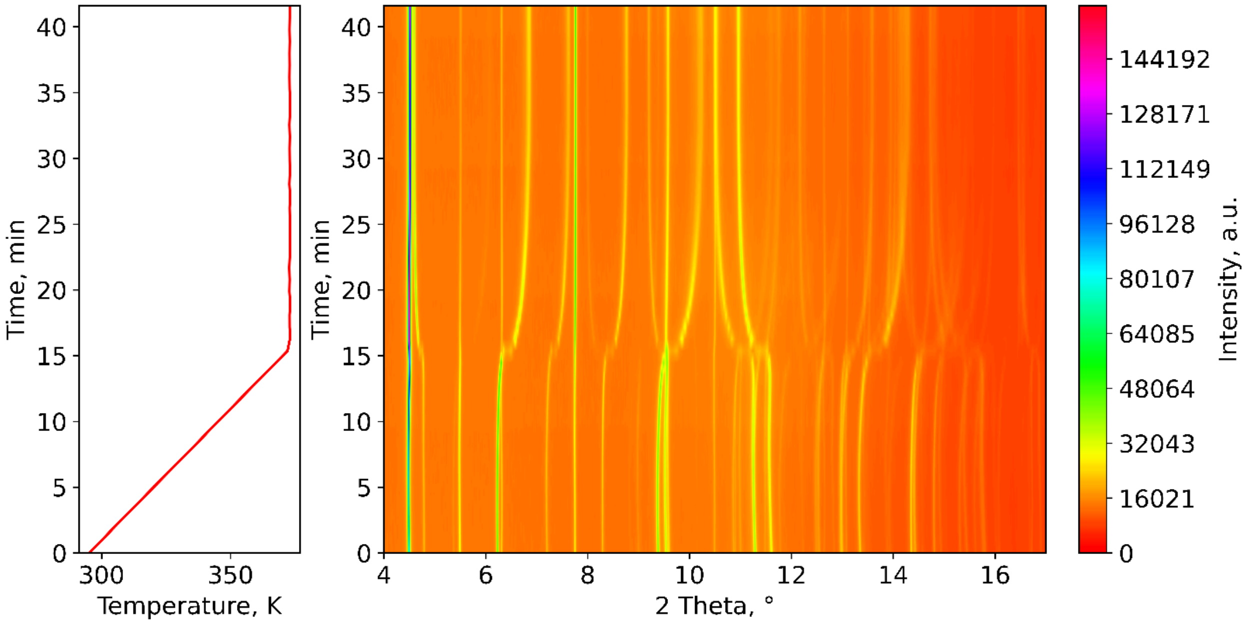

Fig. S9. Counter heating PXRD of ***X-dia-2-Cd-β*** *starting from 298 K to 373 K*

7. Analysis of coordination geometry

1. Coordination environment geometry calculation

Geometry index describes the geometry of the coordination centre; it has values in the range of 0 and 1, where 0 refers the square planar and 1 is tetrahedral geometry. Geometry index for four-coordinated complexes, τ'_4 was calculated by using equation (1) proposed by Okuniewski *et al.* in 2015,[8] where, α and β are two largest angles, and $\beta > \alpha$.

$$\tau'_4 = \frac{\beta-\alpha}{360°-\theta} + \frac{180°-\beta}{180°-\theta} \qquad \textbf{Eqn. 1.}$$

Table S 2. Geometry index calculations.

phase	∠C1-Cd1-C1	∠N1-Cd1-N2	∠C1-Cd1-N1	α	β	**τ'_4**
X-dia-2-Cd-α	115.73	102.36	125.49	115.73	115.73	**0.812154**
X-dia-2-Cd-β	140.2	111.81	102.04	111.81	140.2	**0.677872**
X-dia-2-Cd-γ	116.38	107.61	116.37	116.37	116.38	**0.902451**

2. CSD survey of coordination environment geometry

The list of MOFs having a **dia** net topology was extracted from TTO TOPOS database [9] (version: Dec 2021); valence-bonded MOFs in standard representation were used. 0D subset was obtained by excluding MOF subset[10] from all structures found in CSD database.

ConQuest search (Fig. S10) was performed to determine the angles of the Cd coordination environment (set of 6 angles: N-Cd-C, N-Cd-N, C-Cd-C). Then the τ'_4 was calculated using Eqn. 1 and extracted angle values.

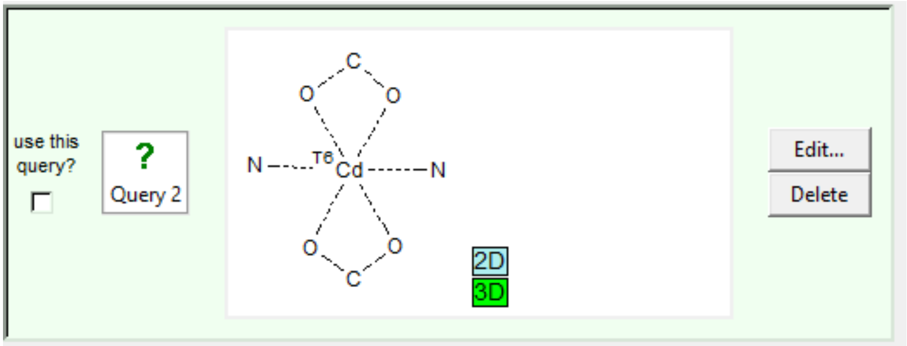

Fig. S10. ConQuest search to determine the angles of Cd coordination environment.

The result of literature survey of the coordination environment geometry are presented in Fig. S11.

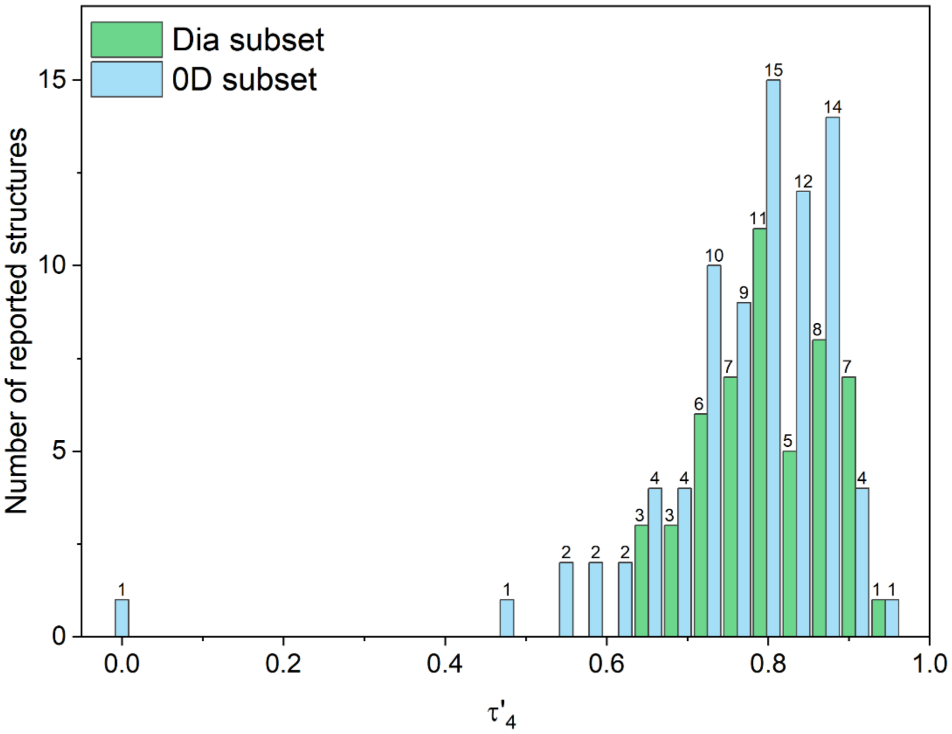

Fig. S11. Calculated τ_4' and corresponding number of reported structures with Cd coordination centre in dia (green) and 0D (blue) subsets.

8. Comparison of structural transformation of X-dia-2-Cd phases

Table S3. Structural transformation comparison between three phases of **X-dia-2-Cd** material.

	X-dia-2-Cd-α	**X-dia-2-Cd-β**	**X-dia-2-Cd-γ**
Angles and distances around Cd atom	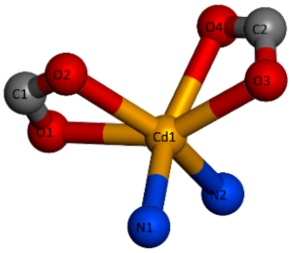 Cd1-O1 : 2.356(Å) Cd1-O2 : 2.347 (Å) Cd1-N1 : 2.251(Å) ∠O1-Cd1-O2 : 55.88 (°) ∠O1-Cd1-O3 : 151.63 (°) ∠O1-Cd1-O4 : 102.65 (°) ∠O2-Cd1-O4 : 91.51 (°) ∠N1-Cd1-O1 : 100.2 (°) ∠N1-Cd1-O2 : 89.12 (°) ∠N1-Cd1-O3 : 97.55 (°) ∠N1-Cd1-O4 : 152.84 (°) ∠N1-Cd1-N2 : 102.40 (°) ∠C1-Cd1-C2 : 115.73 (°) ∠C1-Cd1-N1 : 125.49 (°)	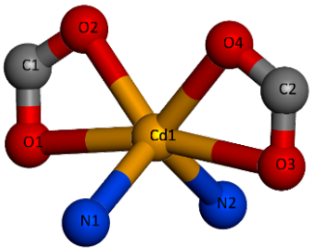 Cd1-O1 : 2.550 (Å) Cd1-O2 : 2.277 (Å) Cd1-N1 : 2.231(Å) ∠O1-Cd1-O2 : 53.11 (°) ∠O1-Cd1-O3 : 167.01 (°) ∠O1-Cd1-O4 : 139.83 (°) ∠O2-Cd1-O4 : 87.15 (°) ∠N1-Cd1-O1 : 85.06 (°) ∠N1-Cd1-O2 : 116.17 (°) ∠N1-Cd1-O3 : 87.66 (°) ∠N1-Cd1-O4 : 111.79 (°) ∠N1-Cd1-N2 : 111.81 (°) ∠C1-Cd1-C2 : 140.20 (°) ∠C1-Cd1-N1 : 102.04 (°)	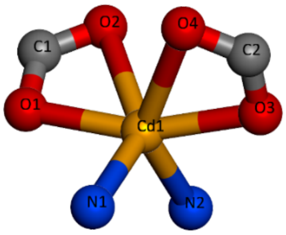 Cd1-O1 : 2.131 (Å) Cd1-O2 : 2.538 (Å) Cd1-N1 : 2.326(Å) ∠O1-Cd1-O2 : 56.08 (°) ∠O1-Cd1-O3 : 160.92 (°) ∠O1-Cd1-O4 : 108.39 (°) ∠O2-Cd1-O4 : 85.76 (°) ∠N1-Cd1-O1 : 88.90 (°) ∠N1-Cd1-O2 : 142.44 (°) ∠N1-Cd1-O3 : 102.41 (°) ∠N1-Cd1-O4 : 94.11 (°) ∠N1-Cd1-N2 : 107.61 (°) ∠C1-Cd1-C2 : 116.38 (°) ∠C1-Cd1-N1 : 116.37 (°)
	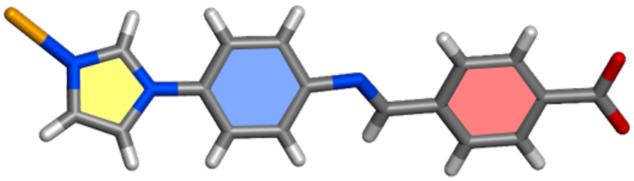		

Angles between 3 planes, corresponding to aromatic rings	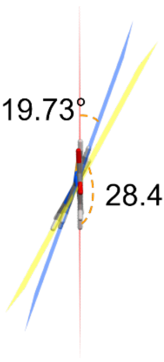	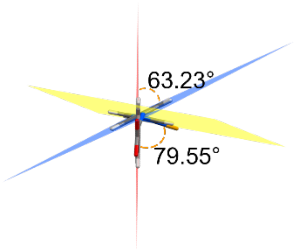 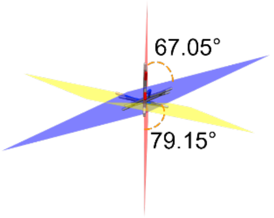	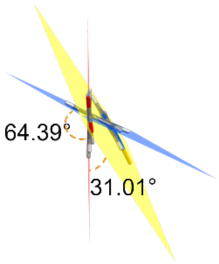
Angles around imine bond	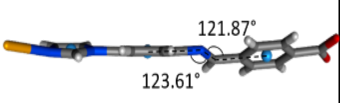	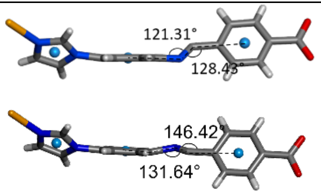	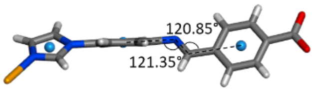
Cd-Cd-Cd angles	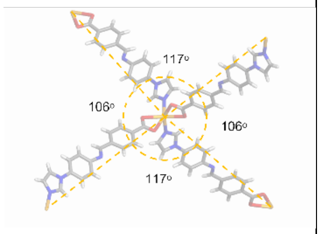	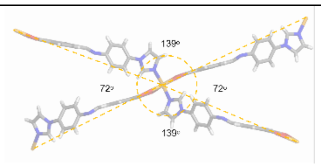	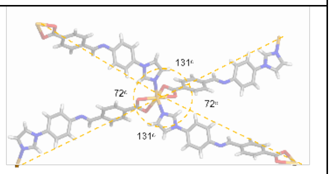
Adamantanoid cage	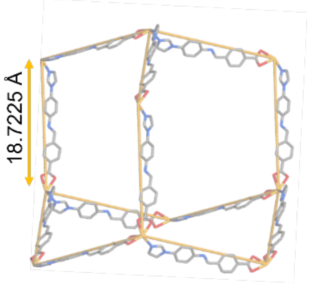	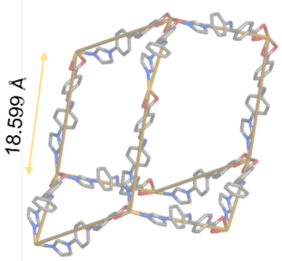	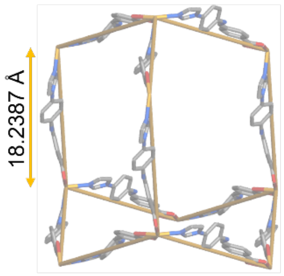
Packing diagrams with and without hydrogens	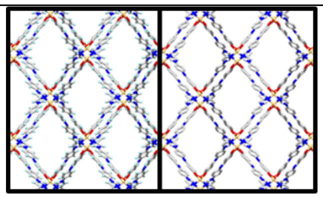	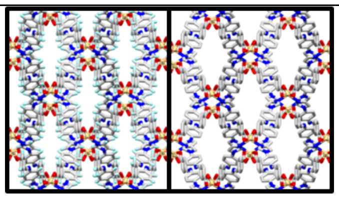	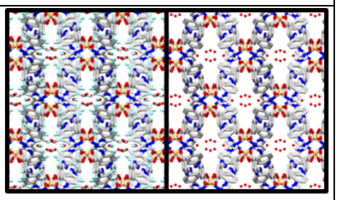

Connolly map along *b*- axes	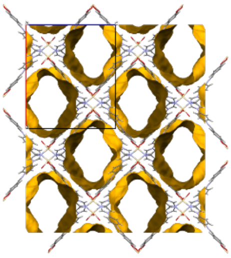	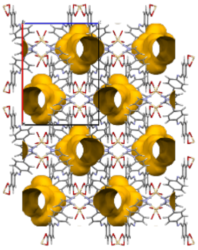	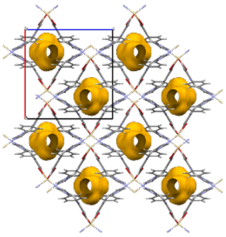
Connolly map along *c*- axes	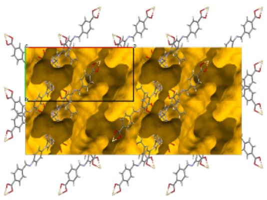	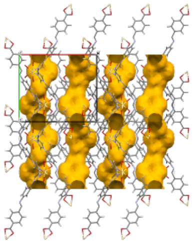	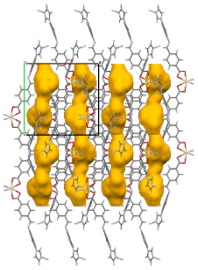

9. Water vapour sorption

1. Water vapour sorption experiment

Water vapour sorption isotherm determination was performed using Adventure Dynamic Vapour Sorption (DVS) instrument manufactured by Surface Measurement Systems. The instrument gravimetrically measures water vapour uptake using air as a carrier gas. Digital mass flow controllers regulate flows of dry and saturated gases. Relative humidity is generated by precisely mixing dry and saturated gas flows in desired flow ratios which produce expected relative humidity. Pure water was used to generate water vapour for these measurements and temperature was maintained at 300 K or at 333 K by enclosing the system in a temperature-controlled incubator. The mass of the sample was determined by a high resolution microbalance Ultrabalance Low Mass with a precision of 0.01 μg. Microbalance has symmetric configuration with two branches of the balance being exposed to the same gas and being kept at the same temperature, which allows negation of buoyancy and drag effects. 400 sccm (Standard Cubic Centimetres per Minute) flow was used for the measurements at 300 K and 50 sccm flow was used for measurements at 333 K. Prior to the measurement, the sample was in-situ activated in dry air at 373 K for 60 minutes using built-in preheater and consequently cooled to sorption temperature in 90 minutes. Isotherm measurements were performed on approximately 12 mg of activated sample. For each isotherm point, $dm/dt < 0.01$ % min^{-1} was used as criteria of reaching equilibrium. Kinetic measurements were performed on 50-100 μm sample fraction obtained by sieving using specified sample mass. 400 sccm min-1 flow was used for the measurements, which is split between two samples. For adsorption and desorption kinetic curves, $dm/dt < 0.05$ % min-1 was used as criteria of reaching equilibrium.

Water vapour sorption cycling was performed at 298 K on a Surface Measurement Systems DVS Intrinsic instrument using air as a carrier gas to gravimetrically measure the uptake and loss of vapour. The mass of the sample was determined by comparison to an empty reference pan and recorded by a high-resolution microbalance with a precision of 0.1 μg. Prior to the measurement, the sample (~10 mg) was *in situ* activated in dry air at 313 K for 60 minutes. Humidity swing was measured between two points 0 and 60 % RH. 100 cycles were subsequently performed, each cycle consisting of 15 min adsorption step (60 % RH) and 30 min desorption step (0 % RH).

$$\frac{dw}{dt} = k \cdot \left(RH_{flow} - RH_{bed}\right) \qquad \textbf{Eqn. 2}$$

where w is uptake (wt.%), k is sorption coefficient, RH_{flow} is relative humidity in the flow and RH_{bed} is relative humidity in sample bed.

Experimental sorption kinetics was modelled using diffusion to sorbent bed surface limitation model recently published by us.[11] Adsorption and desorption kinetics was modelled using Eqn. 2.

RH_{bed} was determined from adsorption branch of the isotherm at the corresponding uptake. Two parameters were fitted: k and t0, where t0 was fitted in 0-3 minutes range.

Table S4. The number of H_2O adsorbed at selected RH % at 300 K.

RH (%)	Uptake (wt %)	Number of H_2O molecules per $Cd(Imibz)_2$
18	2.12	0.81
30	11.22	4.31
60	12.41	5.76
95	15.79	6.06

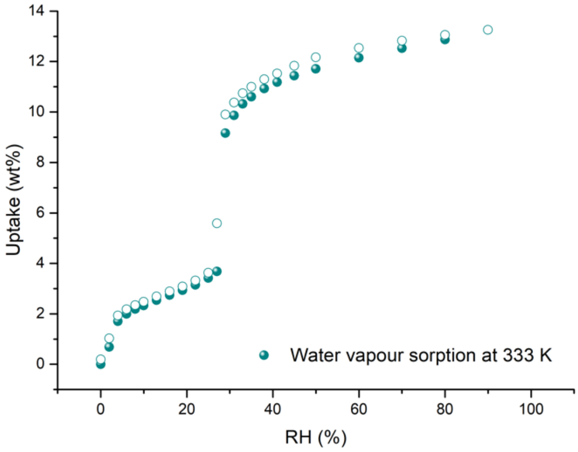

*Fig. S12. Water vapour sorption isotherm for **X-dia-2-Cd** measured at 333 K.*

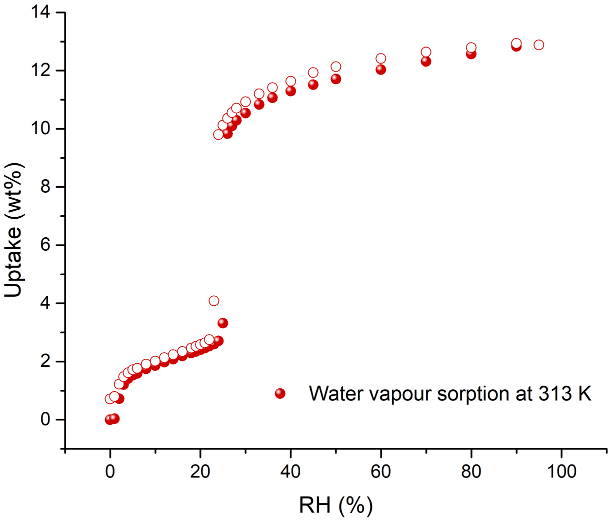

Fig S13. Water vapour sorption isotherm for X-dia-2-Cd measured at 313 K

2. Thermodynamics

1. Enthalpy calculations

Enthalpy for the process:

$$\text{X-dia-2-Cd-}\gamma + H_2O \leftrightarrow \text{X-dia-2-Cd-}\beta\cdot(H_2O) \qquad (\Delta H) \qquad \textbf{Eqn. 3}$$

Was determind using Van't Hoff equation:

$$ln(K) = \frac{-\Delta H}{RT} \qquad \textbf{Eqn. 4}$$

where K is K = (1/P_{gate}) for adsorption and K=(P_{gate}) for desorption, T is temperature in K, and R is gas constant. Enthalpy was determined from the slope of the linear fit (Figs. S14-S15).

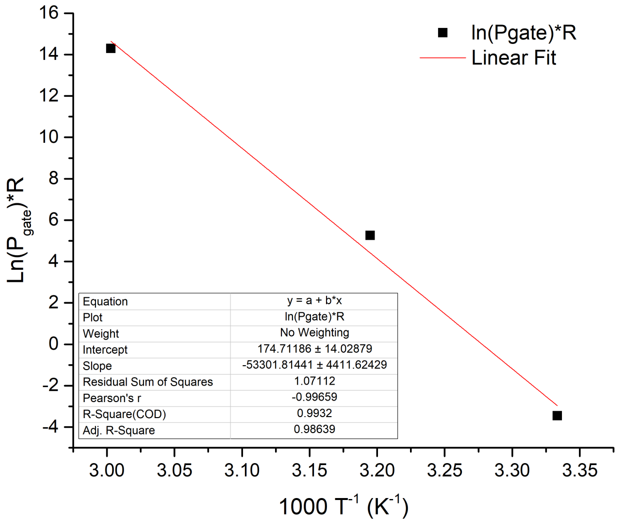

Equation	y = a + b*x
Plot	ln(Pgate)*R
Weight	No Weighting
Intercept	174.71186 ± 14.02879
Slope	-53301.81441 ± 4411.62429
Residual Sum of Squares	1.07112
Pearson's r	-0.99659
R-Square(COD)	0.9932
Adj. R-Square	0.98639

Fig S14. Linear fit of gate adsorption pressure and temperature (1000/T) using the Clausius–Clapeyron equation for X-dia-2-Cd.

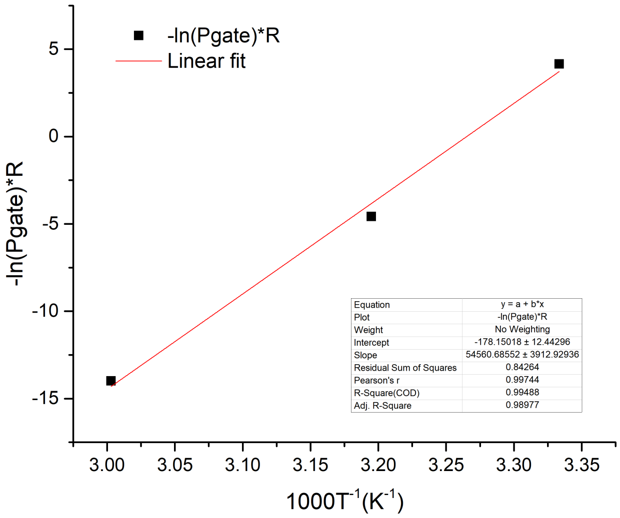

Equation	y = a + b*x
Plot	-ln(Pgate)*R
Weight	No Weighting
Intercept	-178.15018 ± 12.44296
Slope	54560.68552 ± 3912.92936
Residual Sum of Squares	0.84264
Pearson's r	0.99744
R-Square(COD)	0.99488
Adj. R-Square	0.98977

Fig S15. Linear fit of gate desorption pressure and temperature (1000/T) using the Clausius–Clapeyron equation for X-dia-2-Cd.

1. Isosteric heats of adsorption (Q_{st})

Isosteric heats of adsorption (Qst) was calculated using the first step of adsorption branch (before structural transformation is comlepeted) of **X-dia-2-Cd** at multiple temperatures (300, 313 and 333 K). A virial equation of state, Eqn. 5 was used to fit the isotherm of water vapour, where P stands fr pressure in Pa, N is the adsorbed amount in mmolg^{-1}, T is the temperature in K, a_i and b_i are virial coefficients, m and n are the number of coefficients used to describe the isotherms.

$$\ln P = \ln N + \sum_{i=0}^{m} a_i N_i + \sum_{i=0}^{n} \binom{n}{k} b_i N_i$$ **Eqn. 5**

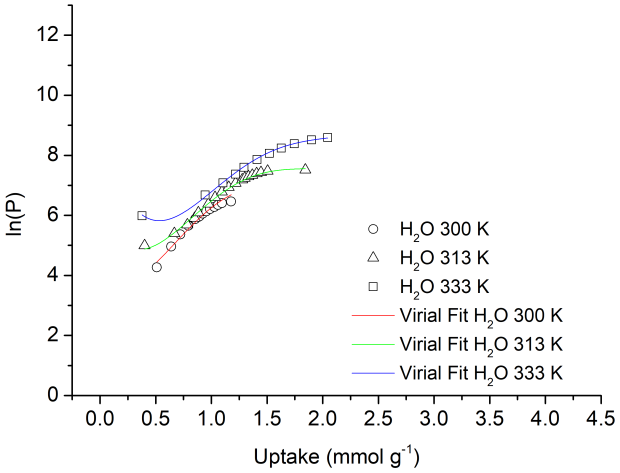

Fig S16. The virial fitting for 300, 313 and 333 K H_2O adsorption on ***X-dia-2-Cd****.*

Table S5. The viral fit parameters for H_2O sorption on ***X-dia-2-Cd****.*

	Value	Standard error
T	300	0
a^{0*}	-14559.7283	2354.87055
a^{1*}	29425.39928	7832.99527
a^{2*}	-18608.78442	9076.58378
a^{3*}	889.27474	5227.81751
a^{4*}	1380.06715	1876.47129
a^{5*}	-127.36721	310.2209
b^{0*}	55.24939	6.71133
b^{1*}	-108.96385	21.31739
b^{2*}	84.20701	20.8258
b^{3*}	-18.89946	6.23379
Adj. R^2	0.99372	

*The viral coefficients a have the unit [K mol^{-i}]

Q_{st} in Figure S17 was calculated from viral model using the Eqn 6, where R stands for the universal gas constant, a_i is virial coefficient, N is adsorbed amount and m is numer of coefficient.

$$-Q_{st} = -R\sum_{i=0}^{m} a_i N_i \quad \textbf{Eqn. 6}$$

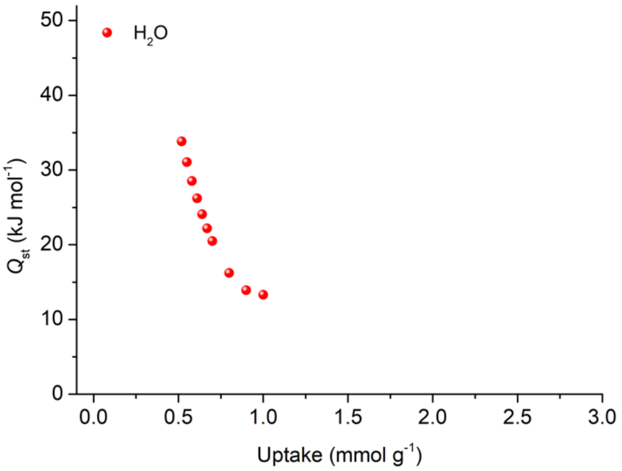

Fig S17. Q_{st} of H_2O by fitting isotherms obtained at 300, 313 and 333 K.

3. Water vapour kinetics

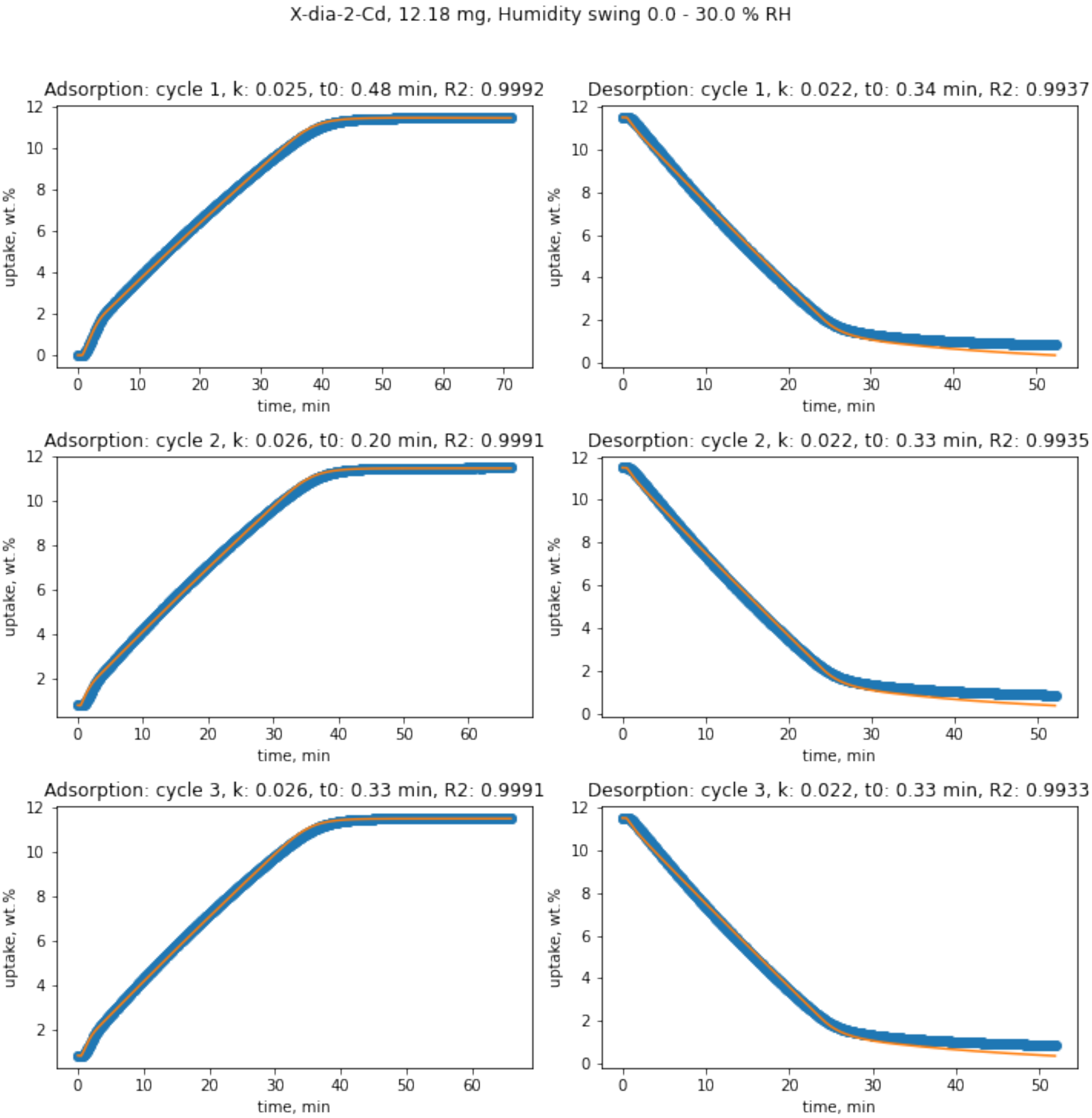

Fig S18. Fit of 0 – 30 %RH humidity swing kinetics data (blue) at 300 K on X-dia-2-Cd sample (12.2 mg) using diffusion to sorbent bed surface limitation model[11] *(orange).*

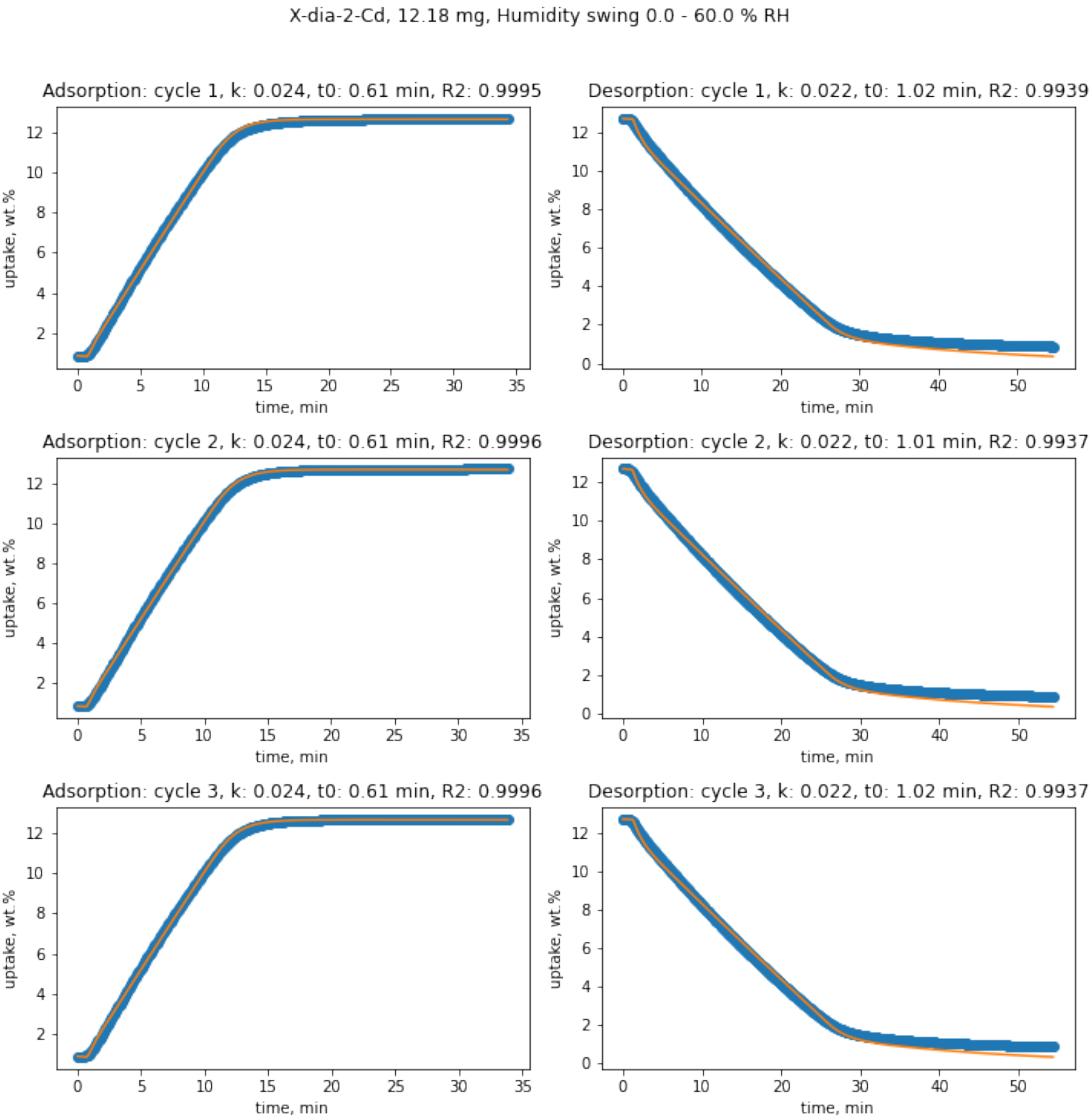

Fig S19. Fit of 0 – 60 %RH humidity swing kinetics data (blue) at 300 K on X-dia-2-Cd sample (12.2 mg) using diffusion to sorbent bed surface limitation model[11] (orange).

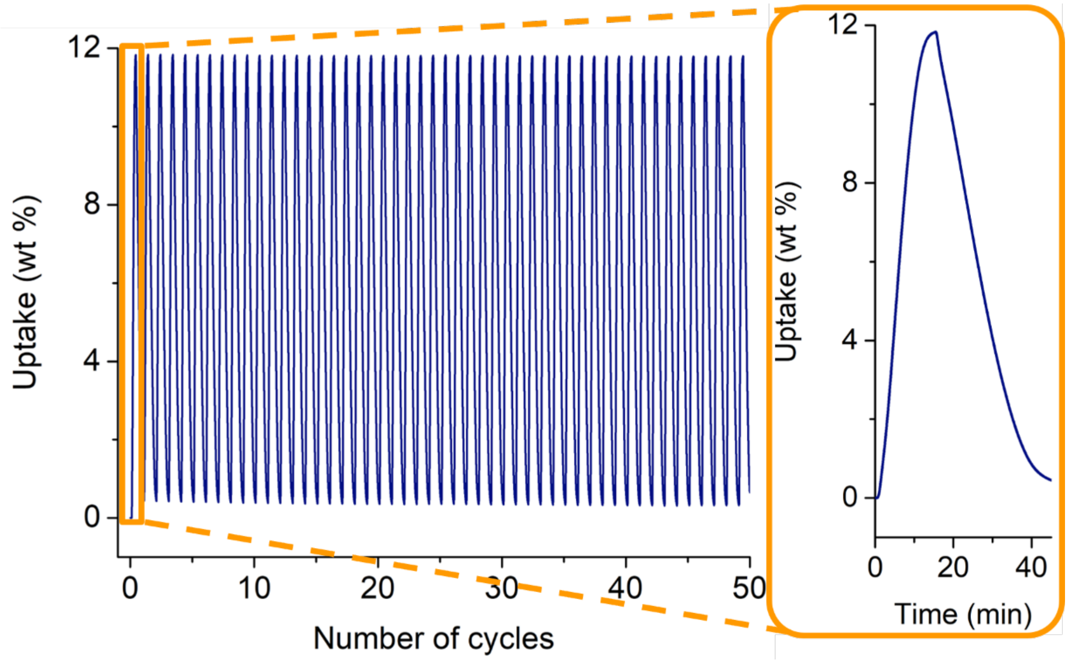

Fig S20. Cycling experiment for ***X-dia-2-Cd-γ*** *under 0-60 % RH humidity swing conditions at 300 K; Inset: expanded view of one adsorption/desorption cycle.*

Table S6. MOMs exhibiting S-shape water vapour sorption isotherms and accompanied by structural transformation

	Sorption isotherm					Temperature-humidity swing		Humidity swing				
Name	Uptake (wt%)	Step (RH, %)	Temperature (K)	Isotherm type[11]	Hysteresis (RH, %)	Cycle number	Conditions	Cycle number	Conditions	Performance (%)	Temperature of water loss from TGA (K)	Reference
SIFSIX-23-Cu	26	-	298	F-I	30.9						433	12
ZF-3	354^{b}	-	308	F-I	12.95	4	298 K, 80% RH – 353 K, 0% RH			100	353	13
ZF-2	520^{b}	-	298	F-I	12.91	4	298 K, 80% RH – 353 K, 0% RH			100	353	13
MIL-53(Al)-OH	42	-	298	F-I	35.03							14
CPL-2	36.7	8.4	300	F-III	5.3							15
[Cu(PF$_6$)$_2$(bpetha)(2,2'- bpy)]n	1^{a}	8.64	298	F-IV	Desorption not complete						373	16
ZPF-2-Co	18	8.87	298	F-IV	2.66			50	298 K, 30% RH – 298 K, 0% RH	96	333	17
{[Cu2(amp)4Cl][Cr(C2O4)3]·6H2O}n	12	10	293	F-II	no			10	293 K, 90% RH – 293 K, 0% RH	100	323	18
{[Cu2(amp)4Cl][Fe(C2O4)3]·6H2O}n	11	10	293	F-II	no						338	18
MIL-53(Cr)	40	12	298	F-IV	8.55						383	19
Co MOF-BP and RP	20.9	14	273	F-IV	Desorption not reported						373	20

[Cu(HQS)(TMBP)]	12	15.1	300	F-IV	10.6	110	300 K, 60% RH – 322 K, 0% RH				313	[21]
[Ce(tci)]n1′	16.8	16	298	F-IV	Desorption not reported						413	[22]
[Co(HL)2]·2H2O	7	17.1	298	F-IV	16.4						413	[23]
X-dia-2-Cd	12	18	300	F-II	no	128	300 K, 60% RH – 333 K, 0% RH	50	298 K, 60% RH – 298 K, 0% RH	100	323	This work
1Mn	25	19.63	298	F-II	4.56			57	298 K, 95% RH – 298 K, 0% RH	100	353	[24]
{[Cd(pzdc)(azpy)]·2H_2O}	90[c]	23.8	298	F-II	22						403	[25]
MIL-53(Al)	8.7	27.79	298	F-IV	14.28						458	[14]
[$Zn_3(L1)_2(L2)(Cl)_4(CH_3OH)_2$]·6$CH_3OH$ (1)	44.79[b]	29.69	298	F-II	17.83					100	343	[26]
[$Zn(H_2SSA)_2$-(H_2O)2]	40.1	33	298	F-IV	Desorption not reported							[27]
CID-6	13	41.7	298	F-III	4.8						423	[28]
DUT-98(3)	28.5	44	298	F-IV	3.82	7	298 K, 100% RH – 353 K, 0% RH			66	353	[29]
[$Zn(3\text{-}tba)_2$]	102[b]	46	298	F-IV	Desorption not completed			5	298 K, 95% RH – 298 K, 0% RH	100	351	[30]
[$Cu(pc1)_2(H_2O)_4$]$(Cl)_2$·8H_2O	23	50		F-IV	45			5	298 K, 80% RH – 298 K, 0% RH	100	333	[31]
MIL-88A@PVDF film	18	50	298	F-II	19.45	20	298 K, 80% RH – 393 K, 0% RH				393	[32]
DUT-98(4)	27.4	50	298	F-IV	2.02						353	[29]

CAU-15-Cit	23.8	50	298	F-IV	Desorption not reported						373	[33]
sql-(azpy)(pdia)-Ni	12	52.5	298	F-II	5			100	298 K, 90% RH – 298 K, 0% RH			[34]
JUK-8	25	52.5	298	F-II	1.59						-	[35]
MIL-53(Al)-ADP	151[b]	55		F-IV	21.015						449	[36]
BUT-8(Cr)A	64.3	65	298	F-II	23.13						653	[37]
CID-5/6	14.3	77.9	298	F-IV	75.9						463	[28]
CID-5	19.2	85.8	298	F-IV	84.2						473	[28]
$[Cu(PF_6)_2(bpetha)_2]n$	2[a]	80	298	F-IV	59.65						373	[16]

[a]mol mol^{-1}; [b]cm^3 g^{-1}, [c]per Cd atom

10. In situ PXRD

In situ PXRD patterns, measured in parallel to carbon dioxide physisorption at 195 K, were collected using a customized Empyrean (Malvern Panalytical GmbH) powder X-ray diffractometer (ω–2θ goniometer, Alpha1 system), equipped with ARS DE-102 closed-cycle helium cryostat. Customized X-ray transparent adsorption cell is based on 1.33″ CF-flange, one part of which is mounted on the cryostat and another is brazed to a beryllium dome. The cell was connected to the low-pressure port of the BELSORP-max (Mictrotrac MRB) volumetric adsorption instrument using 1/8” stainless steel capillary. The TTL trigger was used for establishing the communication between BELSORP-max and Data Collector (Empyrean) software and certified the automated measurement of the adsorption isotherm and PXRD patterns in the selected points of the isotherm. The diffraction experiments were conducted in a transmission geometry (ω–2θ scan mode) in the range of 2θ = 2-70°. Parallel beam optic involving hybrid 2xGe(220) monochromator, primary divergence slits (1/4°) and motorized anti-scatter slits (1/4°), 4 mm mask, Solar slits (0.04°) on the incident and diffracted beam optics. Pixcel-3D detector in 1D scanning mode (255 active channels) was used for counting the signal. A complete CO_2 adsorption–desorption isotherms at 195 K for **X-dia-2-Cd-γ** were measured on 13 mg of the sample and PXRD patterns were *in situ* recorded after equilibration (0.1% of pressure change within 300 s) at selected points of the isotherm.

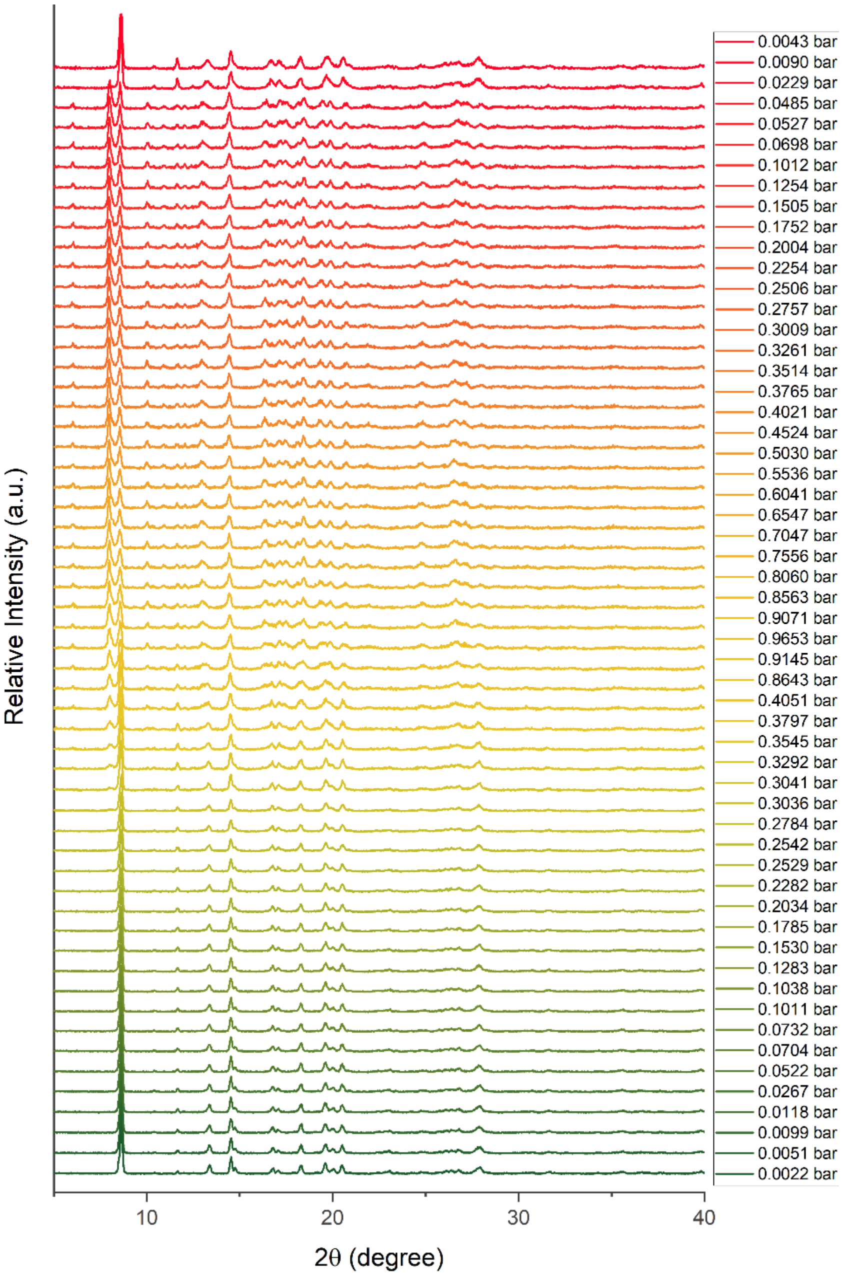

Fig. S21. In situ PXRD measured during adsorption (bottom) and desorption (top) of CO_2 on ***X-dia-2-Cd*** *at 195 K.*

The unit cell parameters of CO_2 loaded **X-dia-2-Cd-δ** were determined from the powder X-ray diffraction patterns collected at 195 K (averaged scans during desorption in pressure range 20-90 kPa). Positions of the first 19 peaks were used for indexing using DICVOL[38] implemented in DASH.[39] Pawley profile fit of powder X-ray diffraction pattern was performed using GSASII.[40]

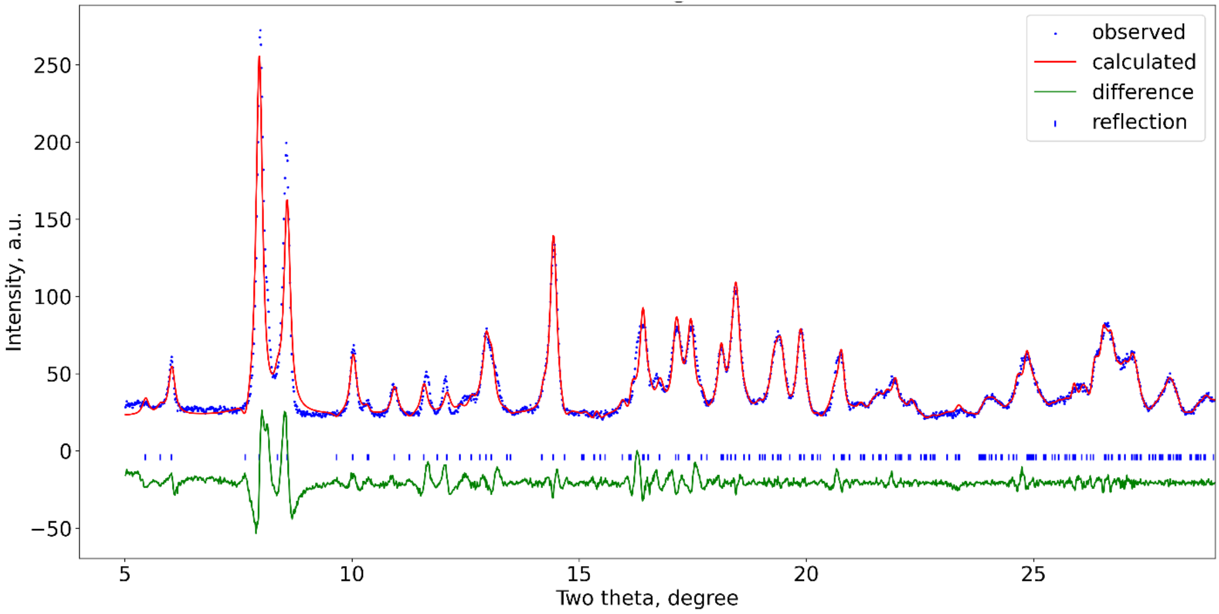

*Fig. S22. Pawley profile fit of **X-dia-2-Cd-δ** at 195 K. Unit cell parameters are: P2, a: 18.737(7) Å, b: 15.266(4) Å, c: 17.184(9) Å, beta: 109.74(15) °, V: 4627(17) Å^3, Rwp = 10.6%.*

11. High pressure gas sorption

A high pressure CO_2 sorption experiment was performed using a Hiden Isochema XEMIS microbalance. An activated sample of **X-dia-2-Cd-γ** was further outgassed under secondary vacuum for 3 hours *in situ* before data were collected. Excess adsorption and desorption profiles were obtained after applying a buoyancy correction using the crystallographically determined density of **X-dia-2-Cd-γ**.

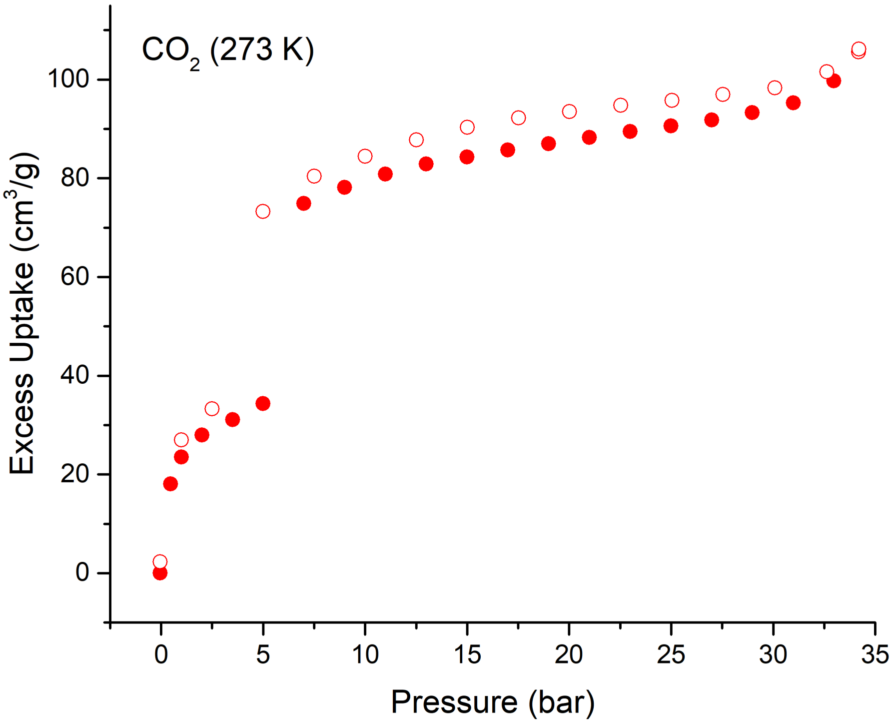

Fig. S23. The high pressure CO2 sorption isotherm for ***X-dia-2-Cd*** *measured at 273 K.*

12. Low pressure gas sorption

A Micromeritics 3Flex surface area and pore size analyser 3500 was used for collecting the 273 K and 298 K sorption isotherms of CO_2, C_2H_2, C_2H_4 and C_2H_6, as well as 195 K isotherms of CO_2 and C_2H_2 and 77 K N_2 isotherms on **X-dia-2-Cd-γ**. The temperature at 195 K and 77 K were maintained using a 4 L Dewar filled with a dry ice-acetone mixture and a liquid nitrogen bath respectively. Bath temperatures of 273 and 298 K were precisely controlled with a Julabo ME (v.2) recirculating control system containing a mixture of ethylene glycol and water. Prior to sorption experiments, a freshly prepared sample of **X-dia-2-Cd-α** was activated on a SmartVacPrep™ using dynamic vacuum and heating for 10 h at 373 K. High grade gases were used as obtained from BOC Gases Ireland Ltd.: He (99.999 %), CO_2 (99.999 %), N_2 (99.9995 %), C_2H_2 (98.5 %), C_2H_4 (99.92 %), C_2H_6 (99 %), C_3H_8 (99.95 %), C_3H_6 (99.5 %) and C_3H_4 (97 %).

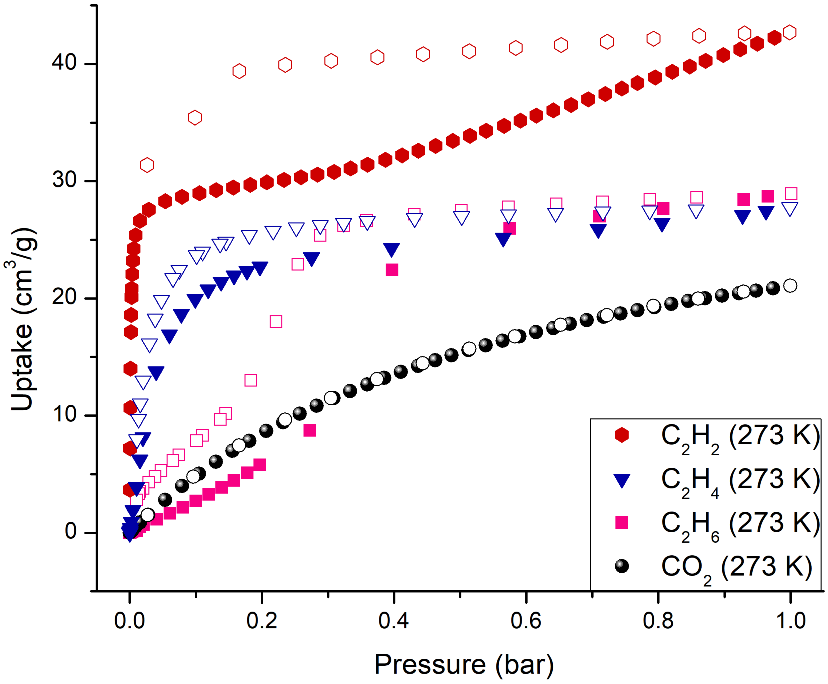

*Fig. S24. Overlaid CO_2 (black), C_2H_2 (red), C_2H_4 (blue) and C_2H_6 (pink) sorption isotherms for **X-dia-2-Cd** measured at 273 K.*

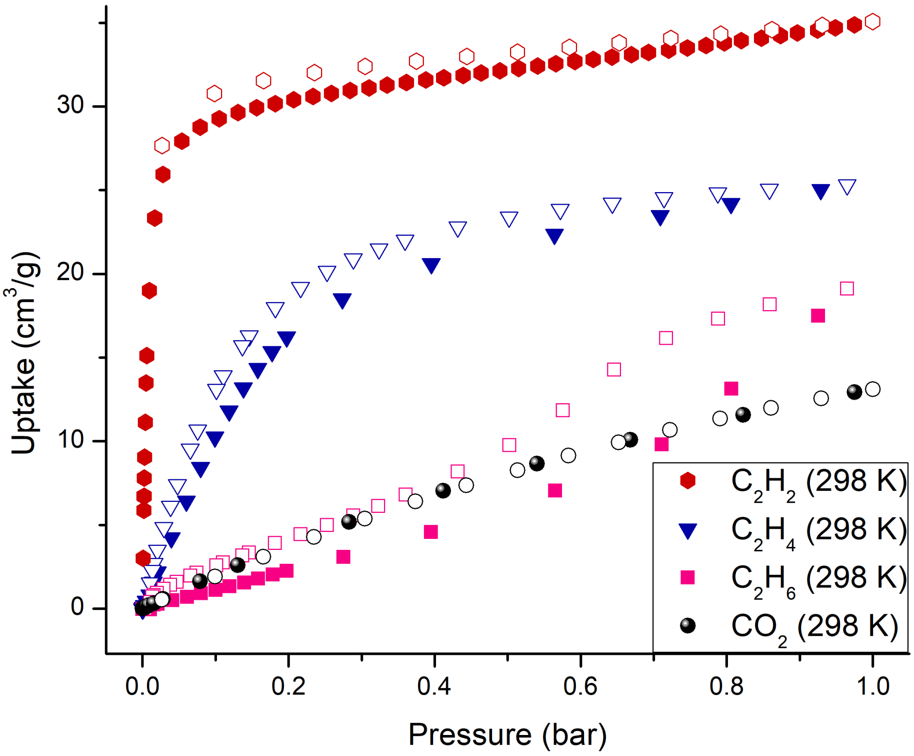

Fig. S25. Overlaid CO_2 (black), C_2H_2 (red), C_2H_4 (blue) and C_2H_6 (pink) sorption isotherms for ***X-dia-2-Cd*** *measured at 298 K.*

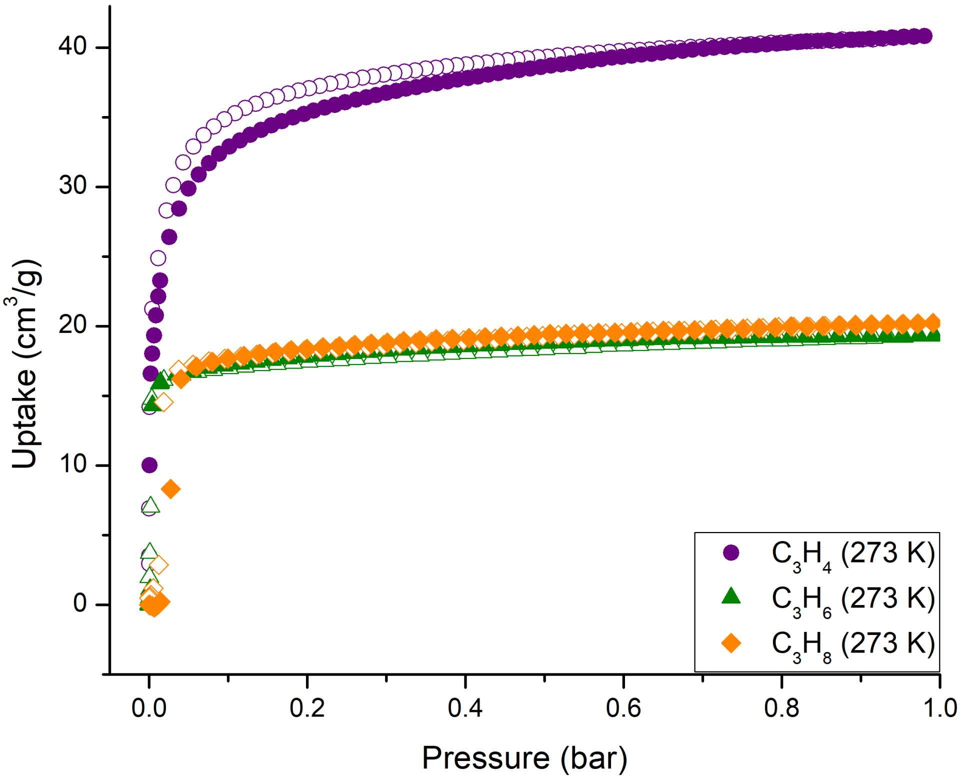

Fig. S26. Overlaid C_3H_4 (purple), C_3H_6 (green)and C_3H_8 (orange) sorption isotherms for ***X-dia-2-Cd*** *measured at 273 K.*

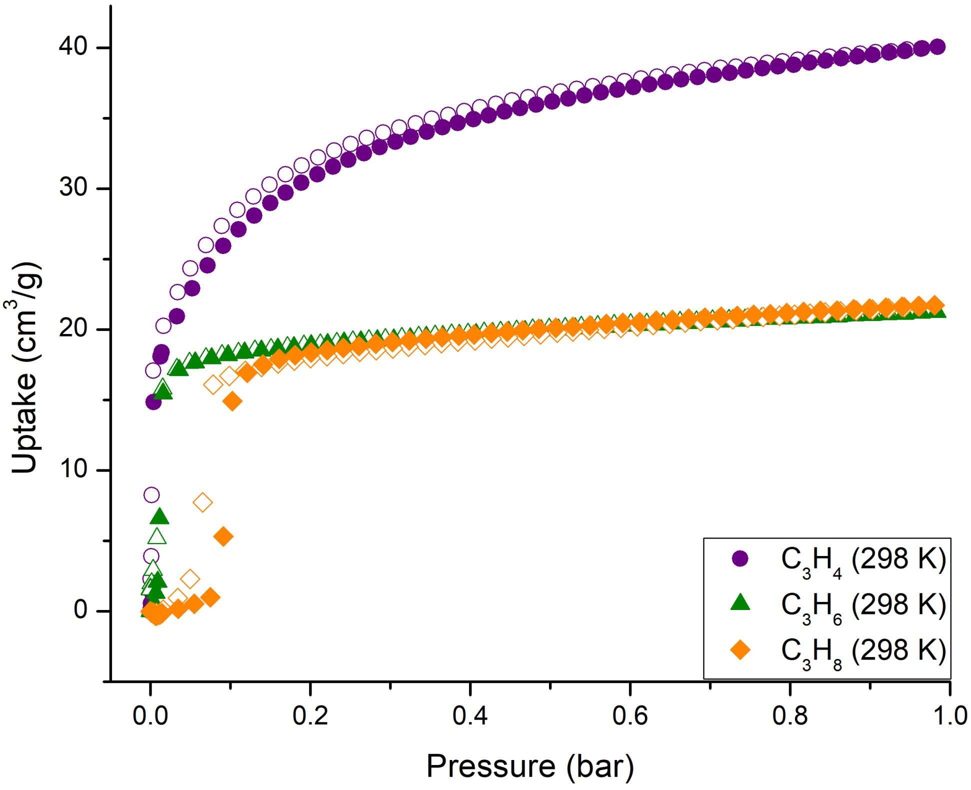

Fig. S27. Overlaid C_3H_4 (purple), C_3H_6 (green)and C_3H_8 (orange) sorption isotherms for ***X-dia-2-Cd*** *measured at 298 K.*

13. Dynamic Column Breakthrough

A Dynamic Column Breakthrough experiment was performed on 410 mg of pre-activated solid sample that was placed in a 1/4 in. stainless steel column to form a fixed bed in a Micromeritics Selective Sorption Analyzer. The gas composition was controlled using an MKS Cirrus 3 mass spectrometer. Prior to the adsorption branch, the bed was purged with a 20 sccm flow of pure He for 3 hours at 333 K and cooled to RT under continuous flow of He. Then, the gas was switched to the targeted C_2H_2/CO_2 mixture with the temperature maintained at 298 K for the adsorption branch of the experiment. Once saturation was achieved, the flow was switched to He at 20 sccm once again, and a temperature ramp rate of 5 K per minute was applied until a steady column temperature of 333 K was achieved. Temperature and He flow were maintained until C_2H_2 and CO_2 outlet concentrations were negligible.

Uptakes were determined from the adsorption branch of the experiments, assuming negligible pressure drop and following Eqn. 7. Dead volume correction was applied by adjusting t_0 to account for time lag between inlet and outlet flows using blank experiments for each inlet mixture composition.

$$q_i = \frac{(V_i t_0 - \int_0^{t_0} V_e dt)}{m} \qquad \textbf{Eqn. 7.}$$

Here in Equation 7, V_i is the inlet flow rate of gas (cm^3 min^{-1}), V, is the effluent flow rate of gas (cm^3 min^{-1}), t_0 is the adsorption saturation time (min) and m is the mass of the sorbent (g). For trace experiments, the adsorbed CO_2 quantity was determined by integrating the area under the CO_2 desorption curve, to minimise error due to residual carrier gas and roll-up during the adsorption branch of the experiment.

The separation factor, α_{AC}=2.32, for the breakthrough experiment for **X-dia-2-Cd-γ** is determined using Eqn. 8, where y_i is the partial pressure of gas i in the gas mixture.

$$a = \frac{q_1 y_2}{q_2 y_1} \qquad \textbf{Eqn. 8.}$$

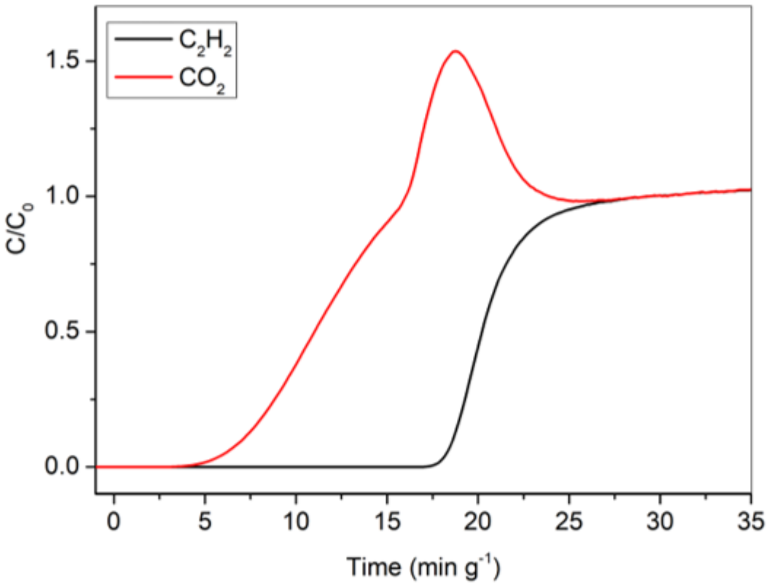

*Fig. S28. Dynamic column breakthrough experiment of binary C_2H_2/CO_2 mixture on **X-dia-2-Cd**.*

*Table S7. Uptakes and separation factors for **X-dia-2-Cd** determined from DCB experiments*

Mass	410 mg
CO_2 flow	0.5 sccm
C_2H_2 flow	0.5 sccm
CO_2 uptake	4.44 cm^3/g
C_2H_2 uptake	10.30 cm^3/g
Separation Factor (α)	2.32

14. Adsorption selectivity calculation

The selectivity for the adsorbate mixture composition of interest were calculated from the single-component adsorption isotherms using Ideal Adsorbed Solution Theory (IAST), implemented in IAST++ program.[41] First, the single-component isotherms for the gas sorbates at 298 K were fitted to the Single-Site Langmuir equation for CO_2 (Eqn. 9) and Dual-Site Langmir equation for C_2H_2 (Eqn. 10).

$$n(P) = q\,\frac{k*P}{1+(k*P)} \qquad \textbf{Eqn. 9}$$

$$n(P) = q_1\frac{k_1P}{1+k_1P} + q_2\frac{k_2P}{1+k_2P} \qquad \textbf{Eqn. 10}$$

In equation 9 and 10, q_i is the amount adsorbed per unit mass of material (in mmol g^{-1}), P is the total pressure (in bar) of the bulk gas at equilibrium with the adsorbed phase, q_1 and q_2 are the saturation uptakes (in mmol g^{-1}) for sites 1 and 2 respectively, k_1 and k_2 are the affinity coefficients (in bar^{-1}) for sites 1 and 2 respectively. Final selectivity for adsorbate *i* relative to adsorbate *j* was calculated using equation 11.

$$S_{i/j} = \frac{(x_i/x_j)}{(y_i/y_j)} \qquad \textbf{Eqn. 11}$$

Here, x_i and x_j are the mole fractions of components *i* and *j*, respectively, in the adsorbed phase, and y_i and y_j are the mole fractions of components *i* and *j*, respectively, in the gas phase.

Table S8. Isotherm fitting parameters and fit R^2 values for IAST calculations.

Adsorbate	**Model**	**R^2**	**q_1 (mmol g^{-1})**	**k_1 (bar^{-1})**	**q_2 (mmol g^{-1})**	**k_2 (bar^{-1})**
CO_2	Single-Site Langmuir	0.999997	1.4847	0.651108	-	-
C_2H_2	Dual-site Langmuir	0.999791	1.663557	0.11619	1.37485*	148.134

*q_2 was limited to 0 to 2 values range.

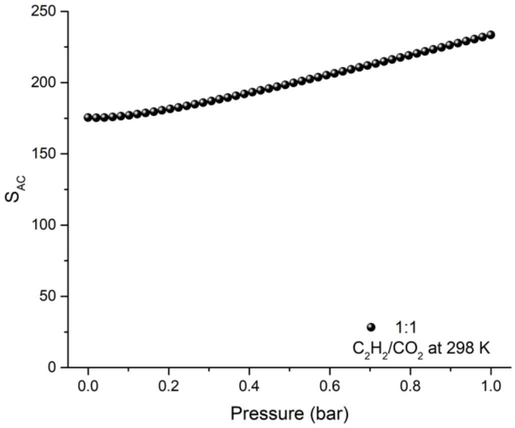

Fig. S29. IAST selectivity for C_2H_2 and CO_2, S_{AC} (equimolar mixture) at 298 K for ***X-dia-2-Cd****.*

15. Survey of crystallographic and topological databases

1. CSD analysis of dia networks

The list of MOFs having dia net topology was obtained from TTO TOPOS database [9] (version: Dec 2021); valence-bonded MOFs in standard representation were used. The enlisted MOM crystal structures from the TTO database were analysed using queries to the Cambridge Structural Database (CSD version 5.43, Jun 2022) through the CSD Application Programming Interface (CSD Python API).[42] The analysis was performed using custom-written Python script which implements the algorithm described by Kumar et al.[43]

The metal-to-linker coordination modes of **dia** nets found by the algorithm are summarized in Fig. S20.

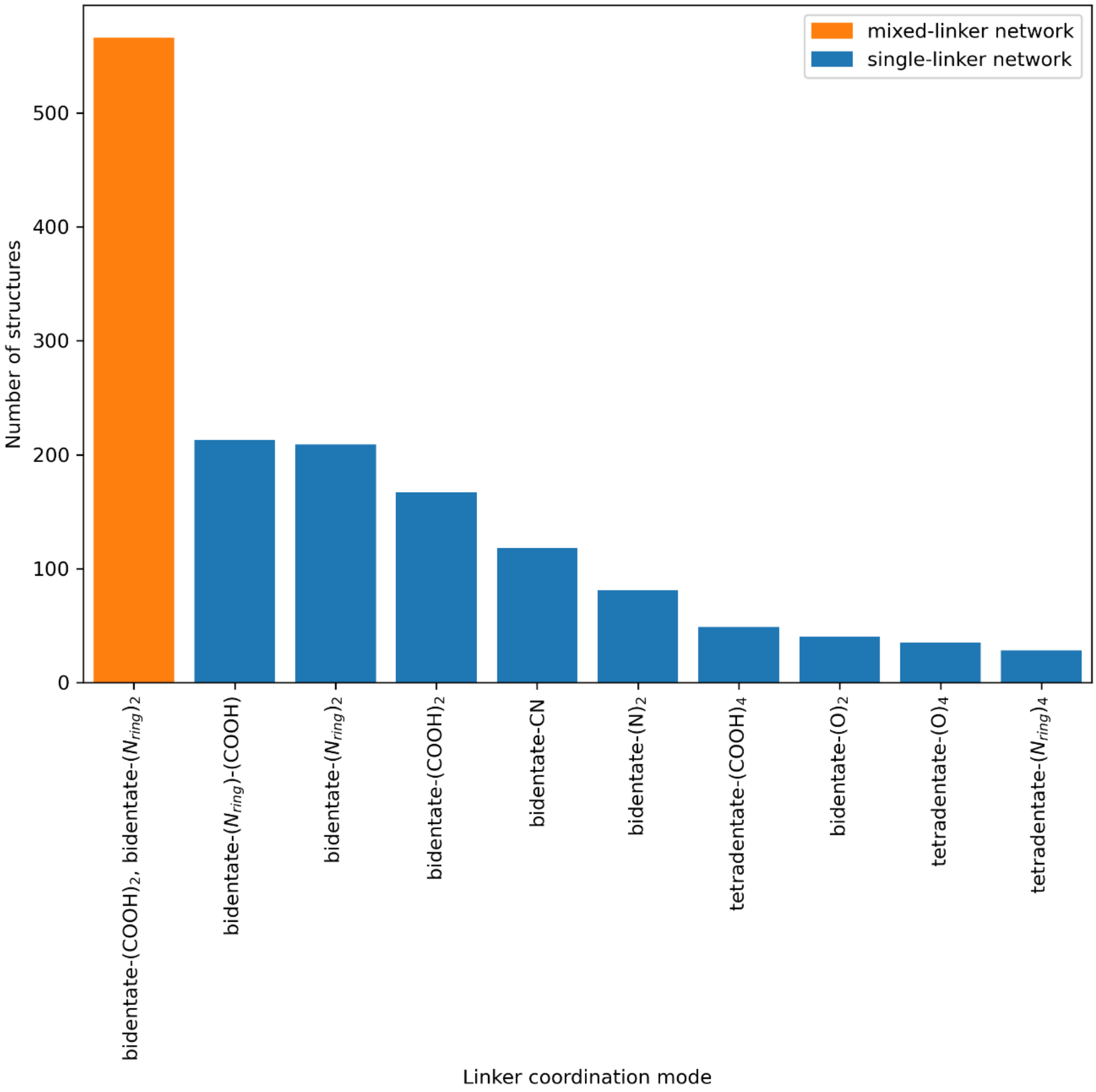

*Fig. S30. Number of **dia** structures reported for different linker coordination modes (top 10).*

1. Analysis of interpenetration in dia networks

For dia nets, network interpenetration was calculated using ToposPro (v. 5.3.3.5).[9] Void volume was calculated using CSD Python API,[42] probe radius 1.2 Å and grid spacing 0.2 Å were used.

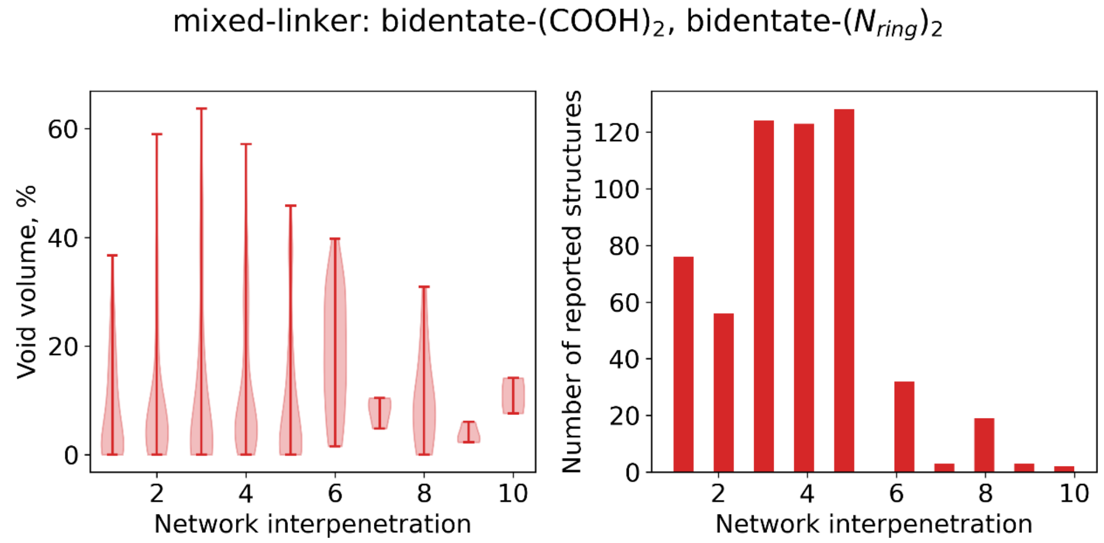
mixed-linker: bidentate-$(COOH)_2$, bidentate-$(N_{ring})_2$

Fig. S 31. Left: Violin plot demonstrating the void space volume of reported structures; right: network interpenetration of the reported MOFs based on mixed-linker (carboxylate linker, N-donor linker).

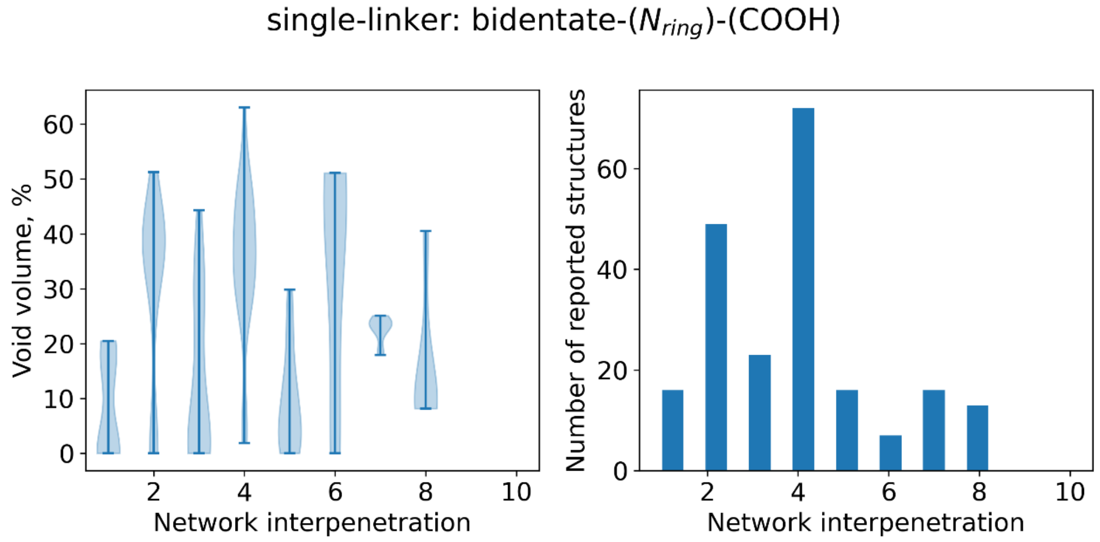
single-linker: bidentate-(N_{ring})-(COOH)

Fig. S32. Left: Violin plot demonstrating the void space volume of reported structures; right: network interpenetration of the reported MOFs based on single (bifunctional) linker.

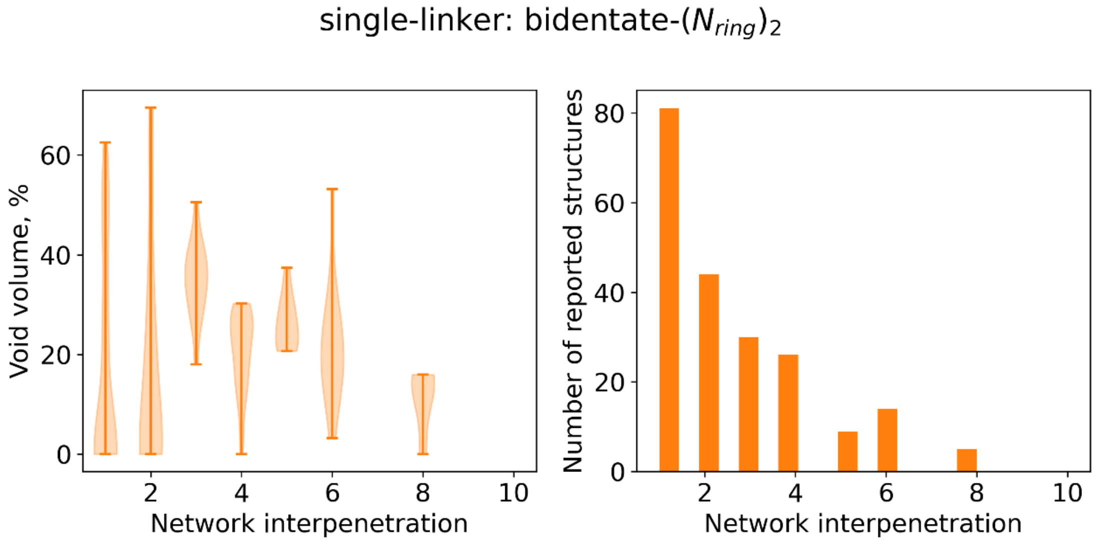

Fig. S33. Left: Violin plot demonstrating the void space volume of reported structures; right: network interpenetration of the reported MOFs based on single (N-donor) linker.

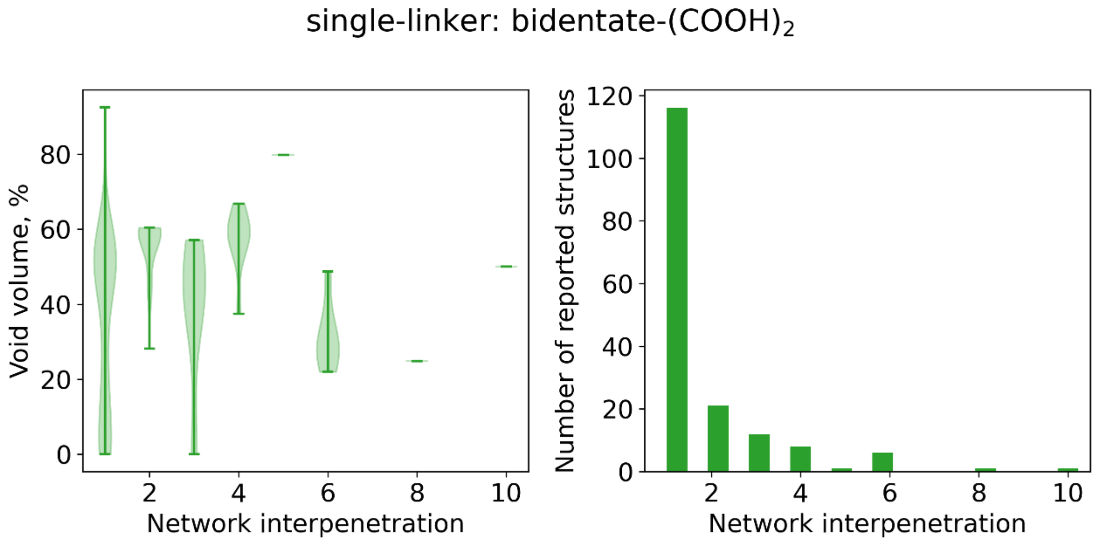

Fig. S34. Left: Violin plot demonstrating the void space volume of reported structures; right: network interpenetration of the reported MOFs based on single (carboxylate donor) linker.

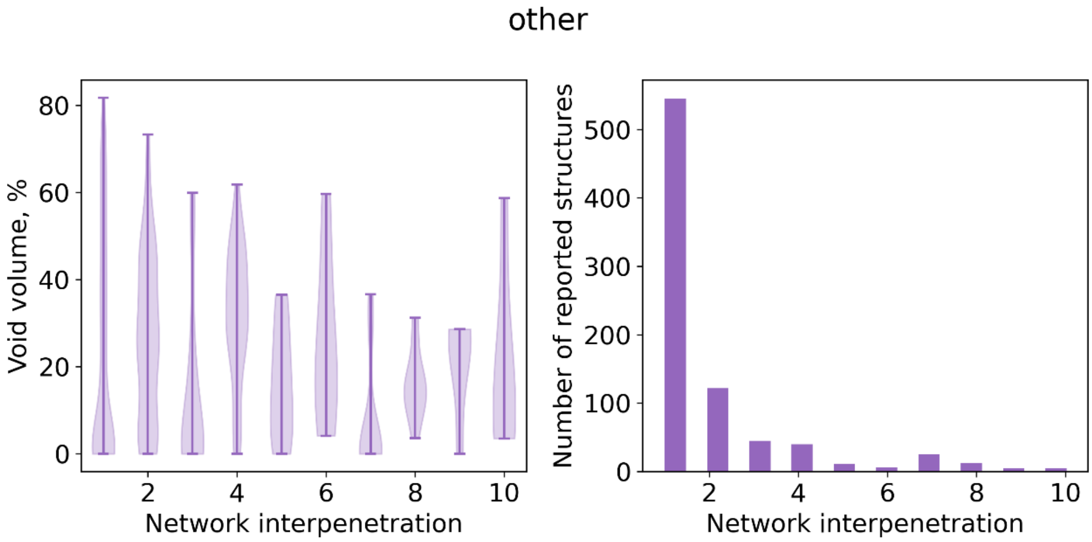

Fig. S35. Left: Violin plot demonstrating the void space volume of reported structures; right: network interpenetration of the reported MOFs based on other linker coordination types.

2. Reported sorption studies for dia structures.

Table S9. Reported sorption studies on dia networks exhibiting flexible isotherms.

Mixed-linker networks:						
Name	Isotherm type^{44}	Absorbate	Temperature (K)	Interpenetration	Organic linker	Reference
flex-MOF(CN)	F-IV	CO_2	196	no	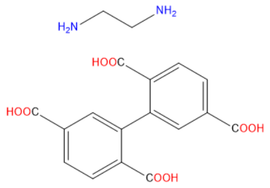	45
flex-MOF(CH^2)	F-IV	CO_2	196	no	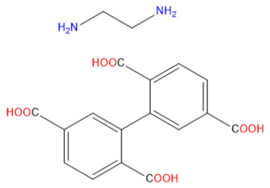	45
[Zn(H2L)(bdc)]·1.4DEF·0.6H2O	F-IV	CO_2	195	3-fold	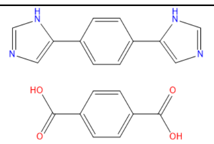	46
ECIT-20	F-II	CO_2	195	3-fold	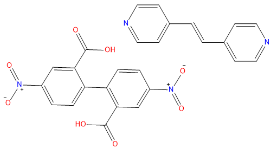	47
JUK-8	F-II	CO_2	195	8-fold	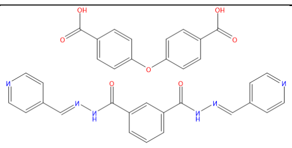	35
[Zn(μ-adipate)(μ-bpa)]·H2O	F-II	CO_2	196	4-fold	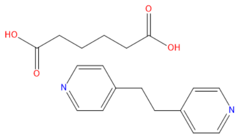	48
[Zn(μ-muconate)(μ-bpa)]·2H2O	F-II	CO_2	196	5-fold	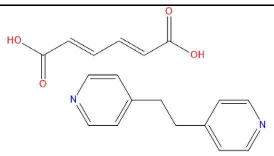	48
[(NiL$_{propyl}$)$_2$(BPTC)]·4DMF·4H_2O	F-II	CO_2	195	no	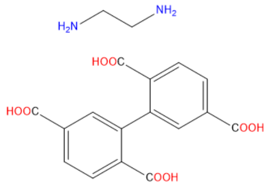	49

$[(NiL)_4(CDTA)_2]\cdot 2.5CH_3CN\cdot 22H_2O$	F-II	CO_2	195	4-fold	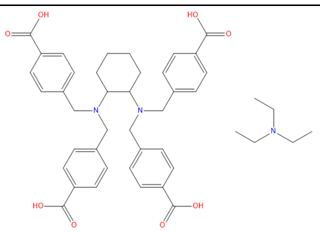	50
$[Zn(4\text{-bpdh})(DHT)]\cdot (MeOH)(H_2O)$	F-IV	EtOH	298	5-fold	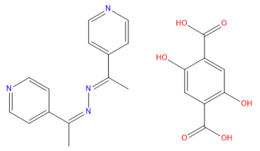	51
Single linker networks:						
$[Cu(pyca)]\cdot 2H_2O$	F-II	H_2O	298	6-fold	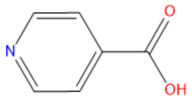	52
$[NH_2(CH_3)_2][In\text{-}(L)_2]\cdot 2.5DMF\cdot 5H_2O$	F-IV	N_2	77	2-fold	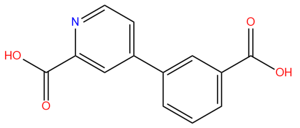	53
Cd-MOF	F-IV	CO_2	195	4-fold	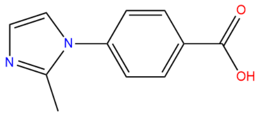	54
X-dia-1-Ni	F-IV	CH_4	298	6-fold	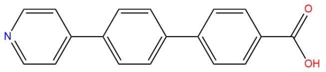	55
$[Co(HLdc)]\cdot 1.5MeOH\cdot dioxane$	F-II	CO_2	195	2-fold	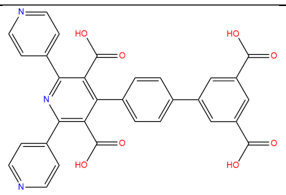	56
ValZnCl	F-II	H_2O	298	2-fold	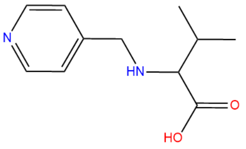	57
$[Zn(Hmpba)_2]\cdot dioxane$	F-II	CO_2	195	4-fold	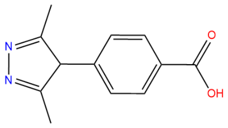	58
$[Zn(Hmpba)_2]\cdot 0.5EtOH\cdot H_2O$	F-IV	CO_2	195	4-fold	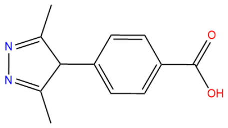	58

$[Zn(CPT)_2](NMF)_3$	F-IV	CO_2	195	4-fold	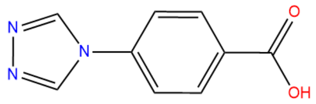	59
$[Cd_2(4\text{-}HIBA)_4]\cdot H_2O$	F-II	CO_2	195	4-fold	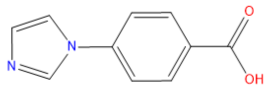	60
SNU-80	F-II	CO_2	195	6-fold	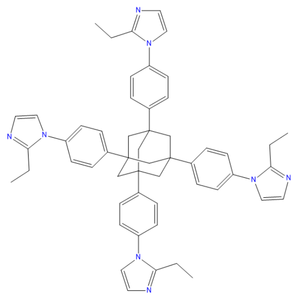	61
$[Co(HL)_2]_3\cdot 2H_2O$	F-II	H_2O	298	6-fold	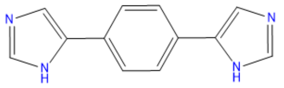	23
MUV-3	F-II	N_2	77	no	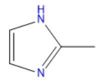	62
$(Me_2NH_2)[In(atp)]_2$	F-II	MeOH	298	2-fold	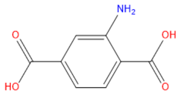	63
$[Me_2NH_2][Eu(ox)_2(H_2O)]$ $\cdot 3H_2O$	F-II	H_2O	298	no	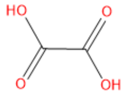	64
SHF-61	F-II	CO_2	298	2-fold	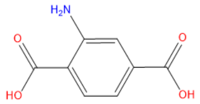	65
InOF-23	F-IV	CO_2	195	2-fold	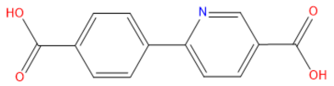	66
NOTT-202a	F-II	CO_2	195	2-fold	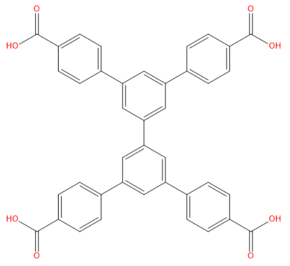	67

X-dia-2-Cd	F-II	CO_2	195	8-fold	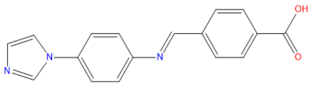	This work

16. References

1. R. Sanii, C. Hua, E. Patyk-Kaźmierczak and M. J. Zaworotko, Solvent-directed control over the topology of entanglement in square lattice (sql) coordination networks, *ChemComm.*, 2019, **55**, 1454-1457.
2. B. A. Inc, Apex4, 2012.
3. L. Krause, R. Herbst-Irmer, G. M. Sheldrick and D. Stalke, Comparison of silver and molybdenum microfocus X-ray sources for single-crystal structure determination, *Journal of Applied Crystallography*, 2015, **48**, 3-10.
4. G. M. Sheldrick, SHELXT - Integrated space-group and crystal-structure determination, *Acta Cryst. A*, 2015, **71**, 3-8.
5. A. L. Spek and Single-crystal structure validation with the program PLATON, *J. Appl. Cryst.*, 2003, **36**, 7-13.
6. T. Degen, M. Sadki, E. Bron, U. König and G. Nénert, The HighScore suite, *Powder Diffraction*, 2014, **29**, S13-S18.
7. S. P. Thompson, J. E. Parker, J. Marchal, J. Potter, A. Birt, F. Yuan, R. D. Fearn, A. R. Lennie, S. R. Street and C. C. Tang, Fast X-ray powder diffraction on I11 at Diamond, *Journal of Synchrotron Radiation*, 2011, **18**, 637-648.
8. A. Okuniewski, D. Rosiak, J. Chojnacki and B. Becker, Coordination polymers and molecular structures among complexes of mercury(II) halides with selected 1-benzoylthioureas, *Polyhedron*, 2015, **90**, 47-57.
9. V. A. Blatov, A. P. Shevchenko and D. M. Proserpio, Applied Topological Analysis of Crystal Structures with the Program Package ToposPro, *Crystal Growth and Design*, 2014, **14**, 3576-3586.
10. P. Z. Moghadam, A. Li, S. B. Wiggin, A. Tao, A. G. P. Maloney, P. A. Wood, S. C. Ward and D. Fairen-Jimenez, Development of a Cambridge Structural Database Subset: A Collection of Metal–Organic Frameworks for Past, Present, and Future, *Chem. Mater.*, 2017, **29**, 2618-2625.
11. A. A. Bezrukov, D. J. O'Hearn, V. Gascón-Pérez, S. Darwish, A. Kumar, S. Sanda, N. Kumar, K. Francis and M. J. Zaworotko, Metal-organic frameworks as regeneration optimized sorbents for atmospheric water harvesting, *Cell Reports Physical Science*, 2023, 101252.
12. B.-Q. Song, Q.-Y. Yang, S.-Q. Wang, M. Vandichel, A. Kumar, C. Crowley, N. Kumar, C.-H. Deng, V. GasconPerez and M. Lusi, Reversible Switching between Nonporous and Porous Phases of a New SIFSIX Coordination Network Induced by a Flexible Linker Ligand, *J. Am. Chem. Soc.*, 2020, **142**, 6896-6901.
13. J. I. Choi, H. Chun and M. S. Lah, Zirconium-formate macrocycles and supercage: molecular packing versus MOF-like network for water vapor sorption, *J. Am. Chem. Soc.*, 2018, **140**, 10915-10920.
14. A. Shigematsu, T. Yamada and H. Kitagawa, Wide Control of Proton Conductivity in Porous Coordination Polymers, *J. Am. Chem. Soc.*, 2011, **133**, 2034-2036.
15. R. Matsuda, R. Kitaura, S. Kitagawa, Y. Kubota, T. C. Kobayashi, S. Horike and M. Takata, Guest Shape-Responsive Fitting of Porous Coordination Polymer with Shrinkable Framework, *J. Am. Chem. Soc.*, 2004, **126**, 14063-14070.
16. S.-i. Noro, K. Fukuhara, K. Kubo and T. Nakamura, Rational construction of wide coordination space and control of adsorption properties in one-dimensional Cu (II) coordination polymer, *Cryst. Growth Des.*, 2011, **11**, 2379-2385.
17. M. Yang, S.-Q. Wang, Z. Liu, Y. Chen, M. J. Zaworotko, P. Cheng, J.-G. Ma and Z. Zhang, Fabrication of Moisture-Responsive Crystalline Smart Materials for Water Harvesting and Electricity Transduction, *J. Am. Chem. Soc.*, 2021, **143**, 7732-7739.
18. P. K. Tsobnang, E. Hastürk, D. Fröhlich, E. Wenger, P. Durand, J. L. Ngolui, C. Lecomte and C. Janiak, Water vapor single-gas selectivity via flexibility of three potential

materials for autonomous indoor humidity control, *Cryst. Growth Des.*, 2019, **19**, 2869-2880.

19. S. Bourrelly, B. Moulin, A. Rivera, G. Maurin, S. Devautour-Vinot, C. Serre, T. Devic, P. Horcajada, A. Vimont and G. Clet, Explanation of the adsorption of polar vapors in the highly flexible metal organic framework MIL-53 (Cr), *J. Am. Chem. Soc.*, 2010, **132**, 9488-9498.
20. Q. Chen, Z. Chang, W.-C. Song, H. Song, H.-B. Song, T.-L. Hu and X.-H. Bu, A Controllable Gate Effect in Cobalt(II) Organic Frameworks by Reversible Structure Transformations, *Angew. Chem. Int. Ed.*, 2013, **52**, 11550-11553.
21. M. Shivanna, A. A. Bezrukov, V. Gascón-Pérez, K.-i. Otake, S. Sanda, D. J. O'Hearn, Q.-Y. Yang, S. Kitagawa and M. J. Zaworotko, Flexible Coordination Network Exhibiting Water Vapor–Induced Reversible Switching between Closed and Open Phases, *ACS Appl. Mater. Interfaces*, 2022, **14**, 39560-39566.
22. S. K. Ghosh, J. P. Zhang and S. Kitagawa, Reversible topochemical transformation of a soft crystal of a coordination polymer, *Angew. Chem. Int. Ed.*, 2007, **46**, 7965-7968.
23. S.-S. Chen, G.-C. Lv, J. Fan, T.-a. Okamura, M. Chen and W.-Y. Sun, Entangled coordination frameworks with 1,4-Di(1 H -imidazol-4-yl)benzene, *Cryst. Growth Des.*, 2011, **11**, 1082-1090.
24. M. Magott, B. Gaweł, M. Sarewicz, M. Reczyński, K. Ogorzały, W. Makowski and D. Pinkowicz, Large breathing effect induced by water sorption in the exceptionally stable nonporous non-MOF crystalline material, 2021.
25. T. K. Maji, K. Uemura, H.-C. Chang, R. Matsuda and S. Kitagawa, Angewandte Chemie International EditionExpanding and Shrinking Porous Modulation Based on Pillared-Layer Coordination Polymers Showing Selective Guest Adsorption, *Angew. Chem. Int. Ed.*, 2004, **43**, 3269-3272.
26. C.-C. Wang, Y.-C. Chung, C.-Y. Liu, G.-H. Lee, S.-Y. Chien, B.-H. Chen and Y.-C. Chuang, Structural characterization and solvent vapor sorption of two solvent-dependent Zn(ii) supramolecular architectures based on a flexible tripodal thioether-based pyridyl ligand and a dicarboxylate-based ligand, *CrystEngComm*, 2023, **25**, 290-298.
27. J. H. Song, D. W. Kim, D. W. Kang, W. R. Lee and C. S. Hong, Humidity-triggered single-crystal-to-single-crystal structural transformations in a Zn (II) coordination polymer displaying unusual activation energy change in proton conductivity, *ChemComm.*, 2019, **55**, 9713-9716.
28. T. Fukushima, S. Horike, Y. Inubushi, K. Nakagawa, Y. Kubota, M. Takata and S. Kitagawa, Solid Solutions of Soft Porous Coordination Polymers: Fine-Tuning of Gas Adsorption Properties, *Angew. Chem. Int. Ed.*, 2010, **49**, 4820-4824.
29. S. Krause, V. Bon, H. Du, R. E. Dunin-Borkowski, U. Stoeck, I. Senkovska and S. Kaskel, The impact of crystal size and temperature on the adsorption-induced flexibility of the Zr-based metal–organic framework DUT-98, *Beilstein J. Nanotechnol.*, 2019, **10**, 1737-1744.
30. M. Deng, S. Mukherjee, Y.-J. Liang, X.-D. Fang, A.-X. Zhu and M. Zaworotko, Water vapour induced reversible switching between a 1-D coordination polymer and a 0-D aqua complex., *ChemComm.*, 2022, **58**, 8218-8221.
31. M. Leroux, G. Weber, J.-P. Bellat, I. Bezverkhyy and N. Mercier, Supramolecular Open-Framework of a Bipyridinium-Carboxylate Based Copper Complex with High and Reversible Water Uptake, *Zeitschrift für anorganische und allgemeine Chemie*, 2016, **642**, 1439-1444.
32. J. Troyano, A. Carné-Sánchez, J. Pérez-Carvajal, L. León-Reina, I. Imaz, A. Cabeza and D. Maspoch, A Self-Folding Polymer Film Based on Swelling Metal–Organic Frameworks, *Angew. Chem. Int. Ed.*, 2018, **57**, 15420-15424.

33. N. Heidenreich, A. Lieb, N. Stock and H. Reinsch, Green synthesis of a new layered aluminium citraconate: Crystal structures, intercalation behaviour towards H2O and in situ PXRD studies of its crystallisation, *Dalton Tran.*, 2018, **47**, 215-223.
34. X. Li, D. Sensharma, V. I. Nikolayenko, S. Darwish, A. A. Bezrukov, N. Kumar, W. Liu, X.-J. Kong, Z. Zhang and M. J. Zaworotko, Structural Phase Transformations Induced by Guest Molecules in a Nickel-Based 2D Square Lattice Coordination Network, *Chem. Mater.*, 2023, **35**, 783-791.
35. K. Roztocki, F. Formalik, A. Krawczuk, I. Senkovska, B. Kuchta, S. Kaskel and D. Matoga, Collective Breathing in an Eightfold Interpenetrated Metal–Organic Framework: From Mechanistic Understanding towards Threshold Sensing Architectures, *Angew. Chem. Int. Ed.*, 2020, **59**, 4491-4497.
36. H. Reinsch, R. S. Pillai, R. Siegel, J. Senker, A. Lieb, G. Maurin and N. Stock, Structure and properties of Al-MIL-53-ADP, a breathing MOF based on the aliphatic linker molecule adipic acid, *Dalton Tran.*, 2016, **45**, 4179-4186.
37. F. Yang, G. Xu, Y. Dou, B. Wang, H. Zhang, H. Wu, W. Zhou, J.-R. Li and B. Chen, A flexible metal–organic framework with a high density of sulfonic acid sites for proton conduction, *Nature Energy*, 2017, **2**, 877-883.
38. A. Boultif and D. Louër, Indexing of powder diffraction patterns for low-symmetry lattices by the successive dichotomy method, *J. Appl. Cryst.*, 1991, **24**, 987-993.
39. W. I. F. David, K. Shankland, J. Van De Streek, E. Pidcock, W. D. S. Motherwell and J. C. Cole, DASH: a program for crystal structure determination from powder diffraction data, *J. Appl. Cryst.*, 2006, **39**, 910-915.
40. B. H. Toby and R. B. Von Dreele, GSAS-II: the genesis of a modern open-source all purpose crystallography software package, *J. Appl. Cryst.*, 2013, **46**, 544-549.
41. S. Lee, J. H. Lee and J. Kim, User-friendly graphical user interface software for ideal adsorbed solution theory calculations, *Korean Journal of Chemical Engineering*, 2018, **35**, 214-221.
42. C. R. Groom, I. J. Bruno, M. P. Lightfoot and S. C. Ward, The Cambridge Structural Database, *Acta Crystallographica Section B Structural Science, Crystal Engineering and Materials*, 2016, **72**, 171-179.
43. N. Kumar, S. Q. Wang, S. Mukherjee, A. A. Bezrukov, E. Patyk-Kaźmierczak, D. O'Nolan, A. Kumar, M. H. Yu, Z. Chang, X. H. Bu and M. J. Zaworotko, Crystal engineering of a rectangular sql coordination network to enable xylenes selectivity over ethylbenzene, *Chem. Sci.*, 2020, **11**, 6889-6895.
44. Q.-Y. Yang, P. Lama, S. Sen, M. Lusi, K.-J. Chen, W.-Y. Gao, M. Shivanna, T. Pham, N. Hosono, S. Kusaka, J. J. Perry IV, S. Ma, B. Space, L. J. Barbour, S. Kitagawa and M. J. Zaworotko, Reversible Switching between Highly Porous and Nonporous Phases of an Interpenetrated Diamondoid Coordination Network That Exhibits Gate-Opening at Methane Storage Pressures, *Angew. Chem. Int. Ed.*, 2018, **57**, 5684-5689.
45. S. Jeoung, S. Lee, J. H. Lee, S. Lee, W. Choe, D. Moon and H. R. Moon, Tuning of the flexibility in metal–organic frameworks based on pendant arm macrocycles, *ChemComm.*, 2019, **55**, 8832-8835.
46. J. H. Park, W. R. Lee, Y. Kim, H. J. Lee, D. W. Ryu, W. J. Phang and C. S. Hong, Interpenetration control, sorption behavior, and framework flexibility in Zn (II) metal–organic frameworks, *Cryst. Growth Des.*, 2014, **14**, 699-704.
47. X. F. Feng, F. Luo, X. F. Yi and A. M. Zheng, Removal and safe reuse of highly toxic allyl alcohol using a highly selective photo-sensitive metal–organic framework, *Green Chem.*, 2016, **18**, 2047-2055.
48. I. H. Hwang, H.-Y. Kim, M. M. Lee, Y. J. Na, J. H. Kim, H.-C. Kim, C. Kim, S. Huh, Y. Kim and S.-J. Kim, Zn-MOFs containing flexible α, ω-alkane (or alkene)-dicarboxylates and 1, 2-bis (4-pyridyl) ethane ligands: CO2 sorption and photoluminescence, *Cryst. Growth Des.*, 2013, **13**, 4815-4823.

49. S.-m. Hyun, J. H. Lee, G. Y. Jung, Y. K. Kim, T. K. Kim, S. Jeoung, S. K. Kwak, D. Moon and H. R. Moon, Exploration of gate-opening and breathing phenomena in a tailored flexible metal–organic framework, *Inorg. Chem.*, 2016, **55**, 1920-1925.
50. P. Ju, L. Jiang and T.-B. Lu, A Three-Dimensional Dynamic Metal–Organic Framework with Fourfold Interpenetrating Diamondoid Networks and Selective Adsorption Properties, *Inorg. Chem.*, 2015, **54**, 6291-6295.
51. B. Bhattacharya, A. Halder, L. Paul, S. Chakrabarti and D. Ghoshal, Eye-Catching Dual-Fluorescent Dynamic Metal–Organic Framework Senses Traces of Water: Experimental Findings and Theoretical Correlation, *Chem. Eur. J.*, 2016, **22**, 14998-15005.
52. T. B. Lu and R. L. Luck, Interlocking frameworks. A consequence of enlarging spacers from 4-pyridinecarboxylate to 4-(4-pyridyl)benzoate, *Inorganica Chim. Acta*, 2003, **351**, 345.
53. B. Zhang, Q.-Q. Chu, K.-F. Yue, S.-H. Zhang, B. Liu and Y.-Y. Wang, A Flexible and Stable Interpenetrated Indium Pyridylcarboxylate Framework with Breathing Behaviors and Highly Selective Adsorption of Cationic Dyes, *Inorg. Chem.*, 2019, **58**, 4019-4025.
54. H. Yang, F. Guo, P. Lama, W.-Y. Gao, H. Wu, L. J. Barbour, W. Zhou, J. Zhang, B. Aguila and S. Ma, Visualizing structural transformation and guest binding in a flexible metal–organic framework under high pressure and room temperature, *ACS Cent. Sci.*, 2018, **4**, 1194-1200.
55. Q. Y. Yang, P. Lama, S. Sen, M. Lusi, K. J. Chen, W. Y. Gao, M. Shivanna, T. Pham, N. Hosono, S. Kusaka, J. J. Perry, S. Ma, B. Space, L. J. Barbour, S. Kitagawa, M. J. Zaworotko and Reversible Switching between Highly Porous and Nonporous Phases of an Interpenetrated Diamondoid Coordination Network That Exhibits Gate-Opening at Methane Storage Pressures, *Angew. Chem. Int. Ed.*, 2018, **57**, 5684-5689.
56. W. Yang, A. J. Davies, X. Lin, M. Suyetin, R. Matsuda, A. J. Blake, C. Wilson, W. Lewis, J. E. Parker and C. C. Tang, Selective CO 2 uptake and inverse CO 2/C 2 H 2 selectivity in a dynamic bifunctional metal–organic framework, *Chem. Sci.*, 2012, **3**, 2993-2999.
57. T. Kundu, S. C. Sahoo, S. Saha and R. Banerjee, Salt metathesis in three dimensional metal–organic frameworks (MOFs) with unprecedented hydrolytic regenerability, *ChemComm.*, 2013, **49**, 5262-5264.
58. C. T. He, P. Q. Liao, D. D. Zhou, B. Y. Wang, W. X. Zhang, J. P. Zhang and X. M. Chen, Visualizing the distinctly different crystal-to-crystal structural dynamism and sorption behavior of interpenetration-direction isomeric coordination networks, *Chem. Sci.*, 2014, **5**, 4755-4762.
59. D. M. Chen, J. Y. Tian, S. M. Fang and C. S. Liu, Two isomeric Zn(II)-based metal–organic frameworks constructed from a bifunctional triazolate–carboxylate tecton exhibiting distinct gas sorption behaviors, *CrystEngComm*, 2016, **18**, 2579-2584.
60. S. S. Chen, Q. Liu, Y. Zhao, R. Qiao, L. Q. Sheng, Z. D. Liu, S. Yang and C. F. Song, New metal-organic frameworks constructed from the 4-imidazole-carboxylate ligand: Structural diversities, luminescence, and gas adsorption properties, *Cryst. Growth Des.*, 2014, **14**, 3727-3741.
61. L. H. Xie, M. P. Suh and Flexible Metal–Organic Framework with Hydrophobic Pores, *Chem. Eur. J.*, 2011, **17**, 13653-13656.
62. Z. Liu, C. Xu, J. Del Pozo, S. Torker and A. H. Hoveyda, Ru-based catechothiolate complexes bearing an unsaturated NHC ligand: effective cross-metathesis catalysts for synthesis of (Z)-α, β-unsaturated esters, carboxylic acids, and primary, secondary, and Weinreb amides, *J. Am. Chem. Soc.*, 2019, **141**, 7137-7146.
63. B. Zhou, T. Zeng, Z. L. Shi, G. Zhang, S. Horike and Y. B. Zhang, An Allosteric Metal–Organic Framework That Exhibits Multiple Pore Configurations for the Optimization of Hydrocarbon Separation, *Chem. Asian J.*, 2019, **14**, 3552-3556.

64. X. Wang, T. Qin, S.-S. Bao, Y.-C. Zhang, X. Shen, L.-M. Zheng and D. Zhu, Facile synthesis of a water stable 3D Eu-MOF showing high proton conductivity and its application as a sensitive luminescent sensor for Cu 2+ ions, *J. Mater. Chem. A.*, 2016, **4**, 16484-16489.
65. E. J. Carrington, C. A. McAnally, A. J. Fletcher, S. P. Thompson, M. Warren and L. Brammer, Solvent-switchable continuous-breathing behaviour in a diamondoid metal–organic framework and its influence on CO2 versus CH4 selectivity, *Nat. Chem.*, 2017, **9**, 882-889.
66. Z. Cao, L. Chen, S. Li, M. Yu, Z. Li, K. Zhou, C. P. Liu, F. Jiang and M. Hong, A Flexible Two-Fold Interpenetrated Indium MOF Exhibiting Dynamic Response to Gas Adsorption and High-Sensitivity Detection of Nitroaromatic Explosives, *Chem. Asian J.*, 2019, **14**, 3597-3602.
67. S. Yang, X. Lin, W. Lewis, M. Suyetin, E. Bichoutskaia, J. E. Parker, C. C. Tang, D. R. Allan, P. J. Rizkallah and P. Hubberstey, A partially interpenetrated metal–organic framework for selective hysteretic sorption of carbon dioxide, *Nat. Mater.*, 2012, **11**, 710-716.